http://dx.doi.org/10.1016/j.ijplas.2019.03.013

Development of the post-form strength prediction model for a high-strength 6xxx aluminium alloy with pre-existing precipitates and residual dislocations

Qunli Zhang [a], Xi Luan [a], Saksham Dhawan [a], Denis J. Politis [a], Qiang Du [b], Ming Wang Fu [c] Mohammad M. Gharbi [d] and Liliang Wang [a*]

[a] Department of Mechanical Engineering, Imperial College London, London, SW7 2AZ, UK

[b] SINTEF Materials and Chemistry, Oslo, Norway

[c] Department of Mechanical Engineering, The Hong Kong Polytechnic University, Hung Hom, Kowloon, Hong Kong, PR China

[d] Schuler Pressen GmbH, Goeppingen, 73033, Germany

Abstract

The applications of lightweight and high strength sheet aluminium alloys are increasing rapidly in the automotive industry due to the expanding global demand in this industrial cluster. Accurate prediction of the post-form strength and the microstructural evolutions of structural components made of Al-alloys has been a challenge, especially when the material undergoes complex processes involving ultra-fast heating and high temperature deformation, followed by multi-stage artificial ageing treatment. In this research, the effects of pre-existing precipitates induced during ultra-fast heating and residual dislocations generated through high temperature deformation on precipitation hardening behaviour have been investigated. A mechanism-based post-form strength (PFS) prediction model, incorporating the flow stress model and age-hardening model, was developed ab-initio to predict strength evolution during the whole process. To model the stress-strain viscoplastic behaviour and represent the evolution of dislocation density of the material in forming process, constitutive models were proposed and the related equations were formulated. The effect of pre-existing precipitates was considered in the age-hardening model via introducing the complex correlations of microstructural variables into the model. In addition, an alternative time-equivalent method was developed to link the different stages of ageing and hence the prediction of precipitation behaviours in multi-stage ageing was performed. Furthermore, forming tests of a U-shaped component were performed to verify the model. It was found that the model is able to accurately predict the post-form strength with excellent agreement with deviation of less than 5% when extensively validated by experimental data. Therefore, the model is considered to be competent for predicting the pre-empting material response as well as a powerful tool for optimising forming parameters to exploit age hardening to its maximum potential in real manufacturing processes.

Keywords: Pre-existing precipitates; Residual dislocations; Constitutive modelling; Age-hardening behaviour; Ultra-fast heating

1. Introduction

A drive for lowering global fuel emissions has led to stricter legislations on manufacturing of lightweight components. Understandably, manufacturers are under increasing pressure to use the most potential and capable materials and optimize the forming processes (Allwood and Shouler, 2009; Lin et al., 2014). Age-hardenable aluminium alloys, e.g. AA6082, are one of the preferred lightweight materials and can be strengthened by post-form artificial ageing processes such as multi-stage paint bake cycles. Modelling the post-form strength of these heat treatable AA6xxx series alloys is especially important, as it enables the optimisation of manufacturing processes and the wide applications of these high strength aluminium alloys. The strength prediction of such alloys, however, is fairly complicated due to multi-parameter dependency on chemical composition, plastic deformation, and post-form heat treatment (Shercliff and Ashby, 1990). Moreover, the overall strength involves the superposition of individual strengthening effects, such as solid solution strengthening, dislocation strengthening, and precipitation strengthening (O R Myhr et al., 2001). Precipitation strengthening is very useful for most commercial AA6xxx alloys, in which the precipitates of various phases exist. The generally accepted precipitation sequence for common Al-Mg-Si alloys in artificial ageing is shown in Fig. 1.

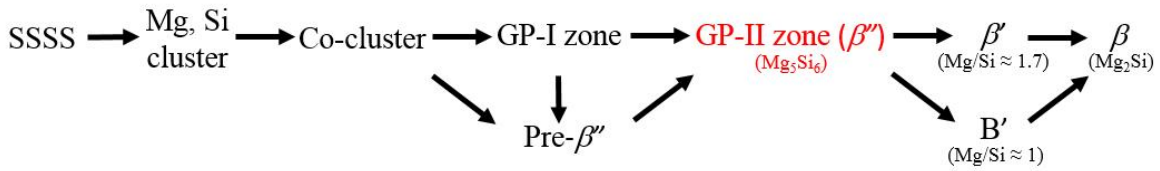

Fig. 1. Precipitation sequence of Al-Mg-Si alloys (Du et al., 2017; Gracio et al., 2004)

As shown in Fig. 1, the precipitation sequence begins with the formation of Si clusters and Mg clusters from supersaturated solid solution. The clusters are then transformed to coherent spherical GP-I zones / pre-β'' precipitates. As artificial ageing proceeds, needle-shaped GP-II zones / β'' (3-4 nm in diameter and 10-20 nm in length) begin to form around nucleation sites, which is associated with the peak strength of material. Subsequently, the formation of semi-coherent rod-shaped precipitate β' will commence signalling an over-aged state. Eventually, equilibrium β phase precipitates are formed leading to a steep decrease in strength.

Modelling the evolution of microstructure was accomplished first by Kampmann and Wagner (Kampmann et al., 1985). The numerical approach was capable of capturing precipitate nucleation-growth-coarsening phenomenon and size distribution by dividing identical particles into size class in the time domain. Later, Shercliff and Ashby proposed a strength model which correlates internal state variables, such as solute concentration, volume fraction of precipitates and radius of precipitates, to model the yield strength evolution during artificial ageing (Shercliff and Ashby, 1990). The hardening phenomenon was considered as a superposition of precipitation hardening (bypassing and shearing), solid solution hardening and intrinsic matrix hardening. Over the last two decades, these classic microstructure and strength models have been further refined and applied to more complicated systems, for instance, transition from shearable to non-shearable precipitates during ageing has been defined and the contribution of non-spherical precipitates has also been embedded (Du et al., 2016; Holmedal et al., 2016; Khan et al., 2008). In addition, extended models were developed to simulate microstructural evolutions for materials under different heat treatment or deformation conditions, such as naturally-aged (Esmaeili et al., 2003a), pre-aged (Esmaeili et

al., 2005), over-aged (Du et al., 2017), cold-deformed (Myhr et al., 2015, 2010) and multistep heat treated (Myhr et al., 2004) conditions.

It is obvious that the above-mentioned models can conveniently simulate the strength evolution of pure as-quenched SSSS, aged (non-deformed) or cold-deformed material during artificial ageing. The published models, however, are currently unable to be used directly to predict the post-form strength of workpieces manufactured through complex processes involving rapid heating and hot/warm stamping. Pre-existing precipitates and residual dislocations induced during the ultra-fast heating, hot forming and quenching processes strongly affect the mechanical properties of aluminium alloys, especially the precipitation response, which makes a new modelling scheme crucial and highly demanded.

It is widely accepted that the presence of the pre-existing precipitates and dislocations would accelerate the precipitation kinetics and have a pronounced effect on the final peak strength (Birol, 2005a; Esmaeili et al., 2005). The pre-existing precipitates consume the solute elements and deplete the supersaturation of the matrix, leading to coarser equilibrium precipitates and shortened time to obtain peak strength. Meanwhile, the introduced dislocations suppress the adverse effects of natural ageing significantly by trapping the quenched-in vacancies and avoiding clustering at room temperature (Kolar et al., 2011; Yin et al., 2016). These residual dislocations also reduce the required activation energy for precipitation and provide heterogeneous nucleation sites for the formation of GP-I zones that readily grow to become stable nuclei for β'' phase (Birol, 2005a; Kolar et al., 2012). Therefore, specifying the initial precipitation state and determining introduced dislocation density during heating and forming are the vital premises to investigate the precipitation sequence.

As desired, the present research addresses the abovementioned issues by establishing a unified post-form strength prediction model (PFS) via considering the effects of induced precipitates and residual dislocations. Dislocation-based viscoplastic constitutive equations and precipitation hardening equations have been developed to model the stress-strain behaviour, microstructural evolution and strength evolution during forming and ageing processes. To predict the strength evolution of the hot-deformed components during multi-stage paint bake cycles utilised (with different paint bake temperatures and paint bake times) in the automotive industry, a time-equivalent method was thus employed to link microstructural variables between different stages of ageing. The developed framework is capable of accurately predicting the post-form strength of AA6082 components manufactured via ultra-fast heating and hot/warm stamping, and can be further used to optimize processing windows in real manufacturing processes.

2. Post-form strength prediction model

The post-form strength of AA6082 specimens undergoing ultra-fast heating and hot/warm stamping is highly dependent on heating rate, target temperature, strain rate, strain level, artificial ageing time and ageing temperature. Consequently, an original post-form strength prediction model, capable of modelling these effects, was introduced. Three distinct sub-models were conceptualized to form the framework of the main model, viz., viscoplastic deformation model, artificial ageing model (with residual dislocations and pre-existing precipitates) and multi-stage ageing model.

2.1 Viscoplastic deformation model

Based on the well-known viscoplastic theory (Csanádi et al., 2014; Kabirian et al., 2015), a set of modified constitutive equations of Eqs. (1) to (5), were used to model the yield stress and the relevant microstructural evolutions during the hot/warm stamping process (Engels et al., 2012; Garrett et al., 2005; Sun et al., 2016; Xiao et al., 2012).

$$\sigma_{total} = E\left(\varepsilon_T - \varepsilon_p\right) \tag{1}$$

$$\dot{\varepsilon_p} = \left(\frac{\sigma - \sigma_{dis} - k}{K}\right)^{n_1} \tag{2}$$

$$\sigma_{dis} = B \cdot \bar{\rho}^{0.5} \tag{3}$$

$$\overline{\rho} = \frac{\rho - \rho_i}{\rho_m} \tag{4}$$

$$\dot{\overline{\rho}} = A_0 \cdot \dot{\varepsilon_p} - A_0 \overline{\rho} \cdot \dot{\varepsilon_p} - C_p \overline{\rho}^{n_2} \tag{5}$$

where n_1, n_2, A_0, A_d, B and C_p are material constants, determined from experimental data. $\sigma_{total}, E, \varepsilon_T, \varepsilon_p, \sigma_{dis}, k, \overline{\rho}$ denote flow stress, Young's modulus, total strain, plastic strain, stress due to dislocation hardening, threshold stress and the normalized dislocation density of material, respectively (Ma et al., 2018; Nieto-Fuentes et al., 2018; Zheng et al., 2018).

Eq. (2) describes the traditional power law formulation of viscoplastic deformation, computing the plastic strain rate by correlating flow stress, dislocation hardening and threshold stress. In Eq. (3), the normalized dislocation density is used to characterize the isotropic hardening phenomenon in the plastic deformation period based on the classic work hardening theory in the following (Hu et al., 2018; Zhang and Ngan, 2018):

$$\sigma_{dis} = \alpha MGb \cdot \rho^{0.5} \tag{6}$$

where α is a material constant, M is the Taylor factor, G is the shear modulus and b is the magnitude of Burgers vector. In Eq. (3), all the material constants are replaced by a single constant B and the normalized dislocation density is used instead, to simplify the calculation of Eq. (6).

The normalized dislocation density is defined in Eq. (4) (Zhan et al., 2011) and ρ_i is the initial dislocation density and ρ_m is the maximum dislocation density the material could generate during deformation. Typically, $\rho_i \ll \rho_m$ and therefore the value of normalized dislocation density is assumed to be in-between 0 and 1. In this method, the evolution of dislocation density is adjusted from different orders of magnitude to a notionally common scale.

In hot stamping process of materials, the dislocation density is affected by the accumulation and annihilation effects (Garrett et al., 2005; Khan et al., 2010, 2009; Zhan et al., 2011; Zhang et al., 2013). Eq. (5) illustrates the normalized dislocation density in a rate form, where the first term ($A_0 \cdot \dot{\varepsilon_p}$) denotes the dislocations generated due to plastic deformation, the second term ($A_0 \overline{\rho} \cdot \dot{\varepsilon_p}$) represents the dynamic recovery of dislocations at elevated temperature and the final term ($C_p \overline{\rho}^{n_2}$) describes the effect of static recovery (Li et al., 2013).

2.2 Artificial ageing model considering pre-existing precipitates and residual dislocations

A refined age-hardening model of Eq. (7) was developed to predict the precipitation response during post-form heat treatment. It considers several important microstructural variables, such as volume fraction, the average radius of precipitates, dislocation density and solute concentration.

$$\sigma_y = f(f_t, r, \rho, C_t) = g(\sigma_{dis},\ \sigma_{ss},\ \sigma_i,\ \sigma_{ppt}) \tag{7}$$

The precipitation of 6000 series aluminium alloy during artificial ageing has been widely investigated and the yield strength is usually computed by the summative contributions of aluminium matrix, solid solution and precipitates (Esmaeili et al., 2005, 2003). Notably, in the refined model, the effect of dislocations is introduced in Eq. (8). The yield strength is then the sum of dislocation hardening contribution σ_{dis}, solid solution strength σ_{ss}, intrinsic strength of the aluminium matrix σ_i and contribution from precipitation hardening σ_{ppt} (including the contributions from shearable precipitates σ_{sh} and bypassing precipitates σ_{by} mechanism). The conversion between hardness and yield strength can be readily expressed by an empirical equation of Eq. (9) (Zhan et al., 2011). A schematic graph of the summative nature of each contribution effect on the yield strength is shown in Fig. 2, which is obtained by running the complete post-form strength prediction model for the material with 10% pre-strain prior to performing artificial ageing at 180°C.

$$\sigma_y = \sigma_{dis} + \sigma_{ss} + \sigma_i + \sigma_{ppt} = \sigma_{dis} + \sigma_{ss} + \sigma_i + \frac{\sigma_{by}\cdot\sigma_{sh}}{\sigma_{by}+\sigma_{sh}} \tag{8}$$

$$HV = 0.33\sigma_y(\text{MPa}) + 22.2 \tag{9}$$

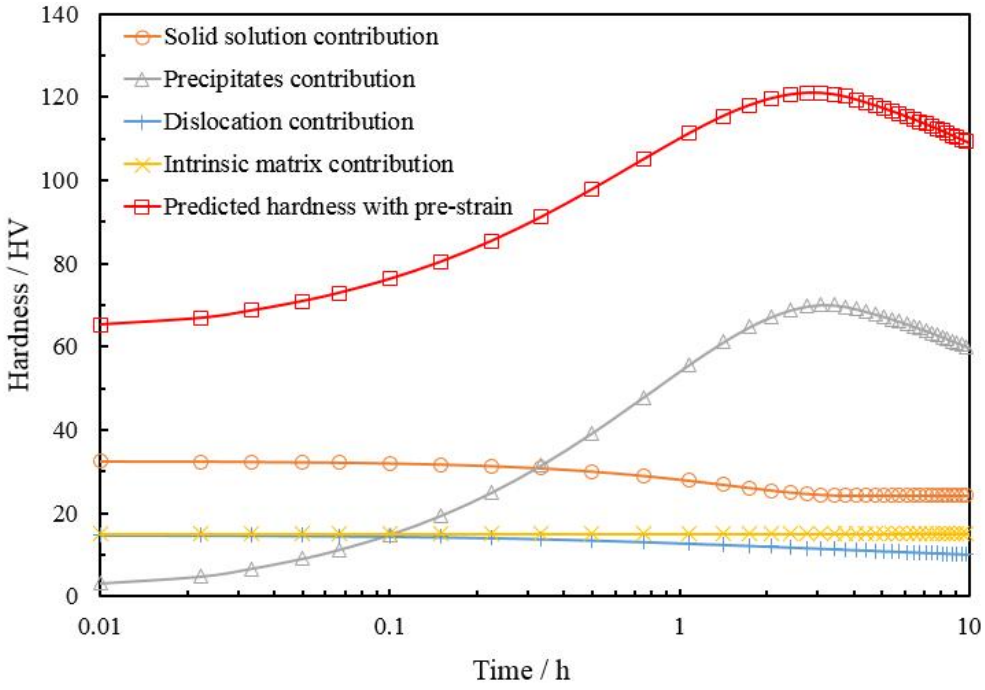

Fig. 2. Contributions of solid solution, aluminium matrix and precipitates to hardness during 180°C ageing with 10% pre-strain

To accurately model the precipitation sequence behaviour, it is necessary to consider the composition of the alloys. AA6082 aluminium alloy is a ternary alloy, where Mg and Si are

the major alloying elements dissolved in the aluminium matrix (Myhr et al., 2004; Shercliff and Ashby, 1990) Most of the solute atoms (including Mg, Si, Mn, Fe, Cu, etc) are re-dissolved in the aluminium matrix after ultra-fast heating and precipitate gradually during subsequent artificial ageing processes. The equilibrium solute concentration depends on the temperature of artificial ageing and represented by Eq. (10).

$$C_e = A_0 \cdot e^{-Q_s/RT} \tag{10}$$

where A_0 is a constant, Q_s is the solvus boundary enthalpy, R is the universal gas constant (8.314 J/mol·K) and T is artificial ageing temperature. When T=T_s, the metastable solid solvus temperature, the maximum solute concentration that can be reached at solvus temperature C_s is (Shercliff and Ashby, 1990):

$$C_s = A_0 \cdot e^{-Q_s/RT_s} \tag{11}$$

Rearranging Eqs. (10) and (11), a new expression of the equilibrium solute concentration at ageing temperature is obtained as follows:

$$C_e = C_s \cdot e^{-\frac{Q_s}{R}\cdot(\frac{1}{T}-\frac{1}{T_s})} \tag{12}$$

During the artificial ageing at elevated temperature, the supersaturation of matrix gradually depletes due to the formation of precipitates. The precipitation kinetics can be described with Shewmon's law (Shewmon, 1963) designated in Eq. (13) and it reveals that the transient solute concentration in the matrix C_t decays exponentially with artificial ageing time t in the following:

$$C_t = C_e + (C_i - C_e) \cdot e^{-\frac{t}{\tau}} \tag{13}$$

$$\tau = k_1 \cdot t_p \tag{14}$$

where C_i stands for initial solute concentration, τ is a temperature-dependent constant indicating the decay speed in Eq. (14). k_1 is a constant and t_p represents the time to achieve the peak strength at a given temperature.

During the entire process, pre-existing precipitates, formed during ultra-fast heating, consume the alloying solute atoms and affect the subsequent artificial ageing response. The initial solute concentration C_i is redefined in Eq. (15) in the following:

$$C_i = C_0 - C_{pep} \tag{15}$$

where C_0 represents the solute concentration of the material in supersaturated solid solution state (SSSS) and C_{pep} refers to the loss of concentration due to pre-existing precipitates.

To better capture the evolution of solute concentration, the format of Eq. (13) is revised to a differential equation:

$$\dot{C}_t = \frac{C_e-(C_0-C_{pep})}{\tau} \cdot e^{-\frac{t}{\tau}} \tag{16}$$

According to Eq. (16), the decay rate of solid solution is mainly determined by temperature-dependent parameters, C_e and τ at a given artificial ageing temperature. For a pre-deformed material, the traditional decay rate equation is no longer suitable to accurately model the evolution of solute concentration due to the effect of dislocations. The presence of dislocations decreases the activation energy of ageing and provides more nucleation sites for precipitates, which accelerates the precipitation response during artificial ageing (Myhr et al., 2015; Saito et al., 2013; Birol, 2005b). Thus, a term controlled by dislocation density as well as a kinetic factor B_1 are formulated to model the effect of pre-existing dislocations in Eq. (17), where the solute loss rate provided by dislocations shows a linear relationship with the normalized dislocation density. For the components without pre-strain, the normalized dislocation density $\overline{\rho}$ equals to zero, which means the decay of solute concentration is purely dominated by Shewmon's law.

$$\dot{C_t} = \left(\frac{C_e-(C_0-C_{pep})}{\tau} \cdot e^{-\frac{t}{\tau}}\right) + B_1 \cdot \overline{\rho} \tag{17}$$

Through measurement of the solute elements dissolved in the aluminium matrix, the volume fraction of precipitates can be evaluated. To simplify the computation process, it is assumed that all precipitates have a constant chemical composition and uniform thermodynamic properties, even though the ratio of Mg to Si could be slightly different. The volume fraction of precipitates, *f*, is then directly proportional to the solute loss in aluminium matrix $C_i - C_t$ in Eqs. (18) and (19) (Esmaeili et al., 2005; Shercliff and Ashby, 1990; Starink and Wang, 2003).

$$\frac{f_t}{C_i-C_t} = \frac{f_e}{C_i-C_e} \tag{18}$$

$$\frac{f_{max}}{f_e} = \frac{C_s}{C_s-C_e} \tag{19}$$

where f_e represents equilibrium volume fraction of precipitates when C_t=C_e and it is the minimum value of f that can be obtained at a certain ageing temperature. f_{max} is the maximum possible volume fraction at absolute zero, when the matrix is purely comprised of aluminium atoms.

By rearranging Eqs. (18) and (19), Eq. (20) is then obtained to express the volume fraction of precipitates during artificial ageing (Shercliff and Ashby, 1990).

$$f_t = f_e \cdot \frac{C_i-C_t}{C_i-C_e} = \frac{f_e \cdot C_i}{C_i-C_e} - \frac{f_e}{C_i-C_e} \cdot C_t = f_{max} \cdot \left(1 - e^{-\frac{t}{\tau}}\right) \cdot [1 - e^{-\frac{Q_S}{R}(\frac{1}{T}-\frac{1}{T_S})}] \tag{20}$$

Accordingly, the volume fraction of precipitates f is transformed into a rate form by differentiating Eq. (20) for accuracy and ease of computation by discretizing into a small time scale. As f is directly related to solute concentration variation, the kinetic factor B_1 is also introduced to quantify the corresponding volume fraction evolution as follows:

$$\dot{f}_t = -\frac{f_e}{C_i-C_e} \cdot \dot{C}_t = -\frac{f_e}{C_i-C_e} \cdot \left(\left(\frac{C_e-C_i}{\tau_1} \cdot e^{-\frac{t}{\tau}}\right) + B_1 \cdot \overline{\rho}\right) \tag{21}$$

For modelling strength evolution, the mean radius of precipitates is another important microstructural parameter. In the early stage of artificial ageing, precipitates grow rapidly with the coherency loss and structural change, and the volume fraction is increased sharply to a high level. The growth rate is subsequently reduced, resulting in the volume fraction approaching the equilibrium value gradually. This precipitation kinetic is approximated based on the classical cubic coarsening law (Shercliff and Ashby, 1990):

$$r^3 - {r_0}^3 = C_1 \cdot \frac{t}{T} e^{-\frac{Q_A}{RT}} \tag{22}$$

where C_1 is the coarsening constant, Q_A is the activation energy for the volumetric diffusion of atoms between particles. r is approximated as the mean radius of circular-section of precipitates through all periods of ageing. Its initial value is the radius of precipitates formed during ultra-fast heating (prior to artificial ageing). Thus, the growth rate of radius of precipitates can be readily obtained from Eq. (22) and designated in the following:

$$\dot{r} = \frac{1}{3}\left(\frac{C_1 \cdot e^{-\frac{Q_A}{RT}}}{T}\right)^{\frac{1}{3}} \cdot t^{-\frac{2}{3}} \tag{23}$$

As mentioned above, it has been found that the pre-deformed Al-Mg-Si alloys experience faster precipitation in the early stage of artificial ageing compared with non-deformed material due to the existence of dislocations. At first, the number density and the size of precipitates increase more rapidly until reaching a dynamic equilibrium, which is accompanied by a decrease of dislocation density (Kolar et al., 2011; Yin et al., 2016). When accounting for the effect of dislocations on precipitate growth, Eq. (23) is not accurate enough to express the coarsening rate for pre-deformed alloys (Poole et al., 2013), as the growth rate of precipitates is proportional to the solute loss from the matrix. Similarly, the kinetic factor B_2 is adopted in Eq. (24) to account for the effect of dislocations.

$$\dot{r} = \frac{1}{3}\left(\frac{C_1 \cdot e^{-\frac{Q_A}{RT}}}{T}\right)^{\frac{1}{3}} \cdot t^{-\frac{2}{3}} + B_2 \cdot \overline{\rho} \tag{24}$$

The second term ($B_2 \cdot \overline{\rho}$) in Eq. (24) captures the accelerated precipitate growth due to dislocations. As artificial ageing proceeds, the effect of dislocations becomes weaker because of the annihilation of dislocations at elevated temperature. Correspondingly, the contribution of the second term is reduced and a dynamic equilibrium is achieved.

$$\dot{\overline{\rho}} = - C_{ageing} \overline{\rho}^{n_2} \tag{25}$$

The normalized dislocation density rate can be computed by using Eq. (25) which is adopted from Eq. (5). Only the static recovery of dislocations is included in the equation because no plastic deformation is involved and thus both strain and strain rate $\dot{\varepsilon_p}$ are zero. C_{ageing} is a material constant and depends on the relationship between static recovery rate and dislocation density during heat treatment.

Fig. 3 shows an example with the evolution of the relevant microstructural variables ($\overline{\rho}$, f and r) for the deformed specimens (SR1, S10%) during artificial ageing at 180°C. It is simulated by using the post-form strength prediction model.

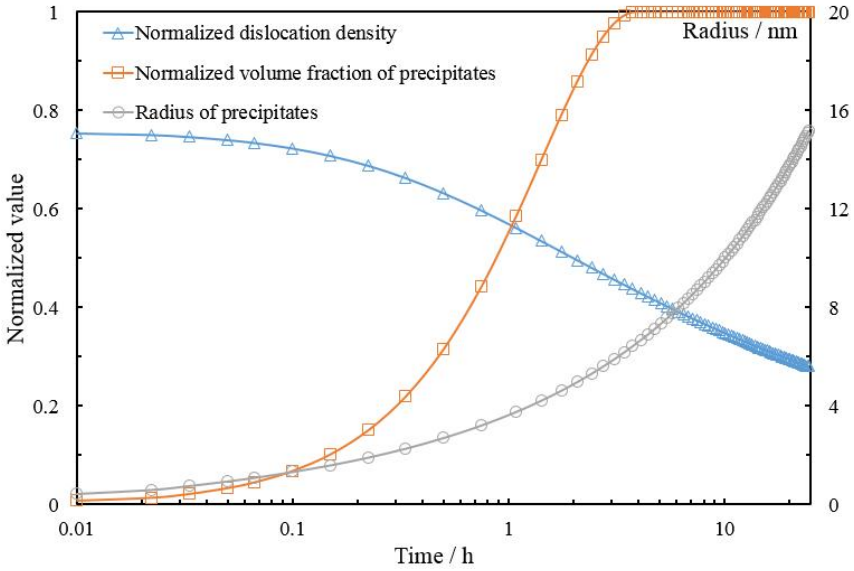

Fig. 3. Microstructural variable evolutions during ageing (180°C, SR1, S10%)

A set of hardening equations were used to model the contribution of dislocations, solute elements, precipitates and aluminium matrix to the yield strength separately by correlating these microstructural variables. As mentioned before, the overall yield strength is the sum of each term and precipitation hardening is a mixture of weak particle hardening (shearing) and strong particle hardening (bypassing). When the average size of particles is small, the interaction between dislocations and precipitates is dominated by particle shearing while bypassing becomes more important as the particles grow larger. The overall contribution of precipitates is designated as the harmonic mean of shearing and bypassing hardening in Eqs. (26-28) (Shercliff and Ashby, 1990). The solute atoms (including Mg, Si, Mn, Fe, Cu, etc) dissolved in the aluminium matrix provide the solid solution hardening. As a ternary alloy, Mg and Si elements are attributed to most of the hardening potential in AA6082 aluminium alloy and the contribution of solutes is summarized in Eq. (29) and the dislocation hardening is expressed in Eq. (30).

$$\sigma_{sh} = C_2 \cdot {f_t}^{1/2} \cdot r^{1/2} \tag{26}$$

$$\sigma_{by} = C_3 \cdot {f_t}^{1/2} \cdot r^{-1} \tag{27}$$

$$\sigma_{ppt} = \frac{\sigma_{by} \cdot \sigma_{sh}}{\sigma_{by} + \sigma_{sh}} \tag{28}$$

$$\sigma_{ss} = \sum_j k_j \cdot {C_j}^{2/3} = C_4 \cdot {C_t}^{2/3} \tag{29}$$

$$\sigma_{dis} = A_d \overline{\rho}^{0.5} \tag{30}$$

where $\sigma_{sh}, \sigma_{by}, \sigma_{ppt}, \sigma_{ss}$, and σ_{dis} represent shearable precipitate hardening, bypassing precipitate hardening, overall precipitate hardening, solid solution hardening and dislocation hardening, respectively. C_2, C_3, C_4, k_j and A_d are material constants. C_2 describes the interaction between the resistance to shear of one particle by moving dislocations, and population and size of the particles; C_3 (C_3=cGb, c is a constant) is the constant to calculate the stress required to bend a dislocation, which combines Burgers vector b and shear modulus G (Shercliff and Ashby, 1990); C_4 is a factor adjusted to the strength of the material in solid solution (Deschamps and Brechet, 1999; Esmaeili et al., 2003b). Cj is the concentration of a

specific alloying element and k_j is the corresponding scaling factor (O. R. Myhr et al., 2001). A_d describes the isotropic hardening due to dislocations at room temperature (Garrett et al., 2005; Khan et al., 2010, 2009; Zhan et al., 2011; Zhang et al., 2013).

2.3 Multi-stage ageing model

The multi-stage artificial ageing model is established based on the idea of equivalent time, which is an important variable associating the microstructural parameters (volume fraction of precipitates and mean radius of precipitates) with the first stage ageing and the second stage ageing. Two-stage ageing is used to demonstrate the modelling approach for multi-stage ageing operations. In the two-stage artificial ageing process, the workpiece is heated to a relatively higher first-stage ageing temperature T_1 to accelerate the ageing response, followed by a second-stage ageing at T_2. The solute concentration is assumed to be the same at the end of first-stage ageing as the beginning of second-stage ageing. The concept of the equivalent time $t_{eq,c}$ is introduced. This term summarizes the effects of first-stage ageing at T_1, enabling the compatibility with the second-stage ageing at T_2 and ensures the consistency between artificial ageing times to be maintained. The solute concentrations when aged at different temperatures are denoted in Eqs. (31) and (32).

$$C_{t1} = C_{e1} + (C_i - C_{e1}) \cdot e^{-\frac{t_1}{\tau_1}} \tag{31}$$

$$C_{t2} = C_{e2} + (C_i - C_{e2}) \cdot e^{-\frac{t_2}{\tau_2}} \tag{32}$$

The equivalent time $t_{eq,c}$ shown in Eq. (34) is then computed by combining the equations above, which assumes that ageing proceeds from $t_{eq,c}$ on the ageing curve for temperature T_2.

$$C_{t1} = C_{t2} \tag{33}$$

$$t_{eq,c} = t_2 = -\tau_2 \cdot \ln\left(\frac{C_{e1}-C_{e2}}{C_i-C_{e2}} + \frac{C_i-C_{e1}}{C_i-C_{e2}} \cdot e^{-\frac{t_1}{\tau_1}}\right) \tag{34}$$

Consequently, the solute concentration during the second-stage ageing is represented by Eq. (35):

$$C_t = C_{e2} + (C_i - C_{e2}) \cdot e^{-\frac{t+t_{eq,c}}{\tau_2}} \tag{35}$$

where t is the time of second-stage ageing.

In the multi-stage ageing process, the average radius of precipitates does not change abruptly when the temperature changes. In order to model precipitate growth, the radius is assumed to remain unchanged during the transition between different stages of ageing, which is illustrated in Eqs. (36) and (37).

$$r_1 = r_2 \tag{36}$$

$$\frac{t_1}{T_1} e^{-\frac{Q_A}{RT_1}} = \frac{t_2}{T_2} e^{-\frac{Q_A}{RT_2}} \tag{37}$$

As shown in Eq. (38), the equivalent time $t_{eq,r}$ is introduced to represent the radius of precipitates in the second-stage ageing and the classical cubic coarsening kinetic is accordingly modified as Eq. (39).

$$t_{eq,r} = t_2 = \frac{T_2}{T_1} \cdot e^{\frac{Q_A}{RT_2} - \frac{Q_A}{RT_1}} \tag{38}$$

$$r^3 - {r_0}^3 = C_1 \cdot \frac{t + t_{eq,r}}{T} e^{-\frac{Q_A}{RT_2}} \tag{39}$$

At higher temperature, the solute elements precipitate faster, and the equilibrium solute concentration is larger during ageing. At higher artificial ageing temperatures, the precipitation rate increases while the equilibrium volume fraction drops. Precipitates are assumed to have a constant chemical composition, hence the volume fraction of precipitates is proportional to the solute loss from the aluminium matrix. For the multi-stage ageing process, the solute concentration and volume fraction of precipitates after first-stage ageing are set as C_x and f_x, generating Eqs. (40) and (41) below:

$$\frac{C_i - C_x}{f_x} = \frac{C_x - C_t}{f_t - f_x} \tag{40}$$

$$f_t = \frac{C_i - C_t}{C_i - C_x} \cdot f_x \tag{41}$$

where f_t, C_t are the corresponding values in the second-stage ageing.

3. Experiments

A series of tests were conducted to investigate the effect of pre-existing precipitates and residual dislocations on the artificial ageing process and then to validate the accuracy of the developed PFS model.

The Al-Mg-Si alloy used in the present investigation was a commercial AA6082 alloy in T4 temper. The as-received material is rolled sheet with thickness of 1.6mm and the chemical composition as shown in Table 1. This is a solute-rich material as the weight percent of Mg and Si is greater than 1%.

Table 1. Chemical composition of AA6082 alloy (wt. %)

Alloy	Al	Mg	Si	Mn	Fe	Cu	Cr	Zn	Ti
AA6082	97.37	0.7	0.9	0.42	0.38	0.08	0.02	0.05	0.03

Axisymmetric dog-bone specimens were machined from the sheet alloy by laser-cutter. High temperature pre-straining tests were conducted in the thermo-mechanical machine Gleeble 3800. K-type thermocouples were welded at the centre of the samples to monitor the temperature evolution of the samples. During pre-straining tensile tests, the workpiece was heated to 450°C and immediately isothermally stretched to certain strain levels (10% and 30%) with various strain rates ranging from 0.01 to 1 s^{-1}. Water quenching was used to subsequently cool the workpiece to room temperature rapidly. Digital image correlation technique was used to measure strain distribution. The schematic shown in Fig. 2 demonstrates the testing process and the related microstructural evolutions. For ultra-fast heating tests, the workpiece was heated to 300, 350 and 450°C rapidly and immediately water quenched to room temperature.

Subsequent artificial ageing, including one-stage and multi-stage ageing, were performed to investigate the effects of pre-straining and ultra-fast heating on the artificial ageing responses. In the one-stage artificial ageing (AA) tests, the workpiece was heated to a target temperature with a range from 190 to 240°C. The required ageing time is reduced with the increasing

ageing temperature. In order to capture the full strength evolutions, the ageing time at 190, 220 and 240°C is 16, 3.5 and 1h, respectively. In the two-stage AA tests, the material was held at 220°C for 3-6 min in the first stage and then followed by a second-stage ageing at 190°C for 20, 40, 120 and 240 min. The resulting specimen hardness was measured with a Zwick hardness tester. All hardness measurements were made by using a 30N (HV3) load and 10s dwell time at room temperature. For each specimen, at least three indentations were performed to obtain an average value of hardness.

Microstructure investigations were conducted on an FEI Technai F20 transmission electron microscope (TEM). After electropolishing, the disc-shaped samples with a diameter of 3mm were punched from the ground slice. Ion thinning was conducted by Gatan 691. For each TEM sample, more than 50 images in different scales were taken in order to measure the radius, number density and volume fraction of precipitates. All images were preferentially acquired along the ⟨100⟩ Al-zone axis, where the distribution of precipitates can be readily observed.

Furthermore, forming test was conducted to form a U-shape component by using the prototype production line, Uni-Form (Luan et al., 2016). The blank was conduction heated to target temperature by top and bottom platens at an ultra-fast rate and transferred via conveyer belts to the dies for stamping. Quenching is completed in cold dies to ensure the critical quenching rate can be achieved (Wang *et al*. 2017; Luan *et al*., 2016). Post-form artificial ageing was subsequently performed to enhance the mechanical properties of the formed workpiece. The comparison is presented in Section 4.5.

4. Results and discussion

The effects of pre-existing precipitates, residual dislocations and multi-stage artificial ageing on post-form strength are discussed alongside the results of relevant experimental procedures. The verification of the developed model is then provided, with the error bars, against the stamped U-shaped component.

4.1 Effect of pre-existing precipitates on the post-form strength

The results of the hardness evolution with target temperature against ageing time are shown in Table 2. Tests were conducted under a fast heating rate of 50°C/s to the target temperatures of 300, 350 and 450°C, followed by water quenching and artificial ageing at 180°C for a range of times. As shown in Table 2, after fast heating and water quenching, the hardness values are lower than the hardness of the initial T4 temper (80.0HV), but higher than the pure SSSS material (48HV). It also indicates that the peak hardness occurred after approximately 6h ageing for the specimen that was rapidly heated to 450°C while it took 3.5h to reach peak condition when heated to 300 and 350°C. In addition, the peak hardness of all samples after ageing can be recovered at least 92% of the T6 temper value.

Table 2. Hardness values of the specimens after the 180°C artificial ageing with different target heating temperatures

Target heating temperature / °C	Hardness / HV						
	0h AA	0.67h AA	1.33h AA	3.5h AA	6.5h AA	10.75h AA	15.75h AA
300	60.9	111.9	118.6	119.9	118.6	116.1	108.8
350	59.5	97.8	109.4	112.4	110.6	107.1	102.8
450	56.9	106.0	116.5	119.6	121.8	118.9	112.3

Figs. 4. (a), (b) and (c) show the TEM scans performed on specimens after ultra-fast heating to the target temperatures of 300, 350 and 450°C, and followed by water quenching. Dot-like precipitates with the average radius of approximately 3.9 nm, are observed and found to be relatively finely dispersed in the aluminium matrix. The lowest precipitate density was found when heated to 450°C while the highest density was observed in the 350°C specimen. EDXS (Energy-dispersive X-ray spectroscopy) tests were conducted to determine the chemical composition of the observed spherical precipitates. The Mg: Si ratio lies between 1 and 1.5 by analysing the results.

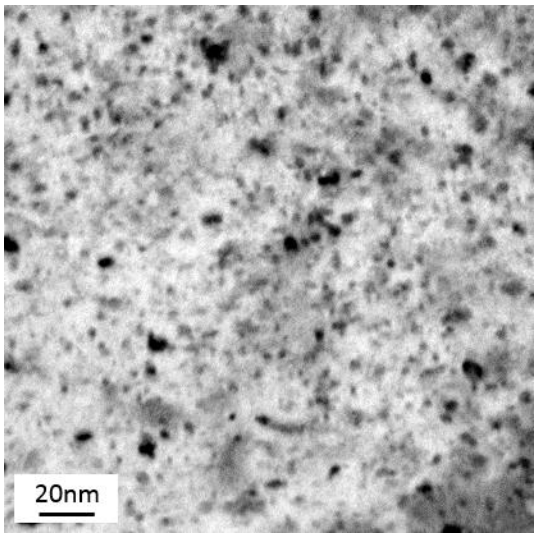

(a). Fast heating to 300°C +water quenching

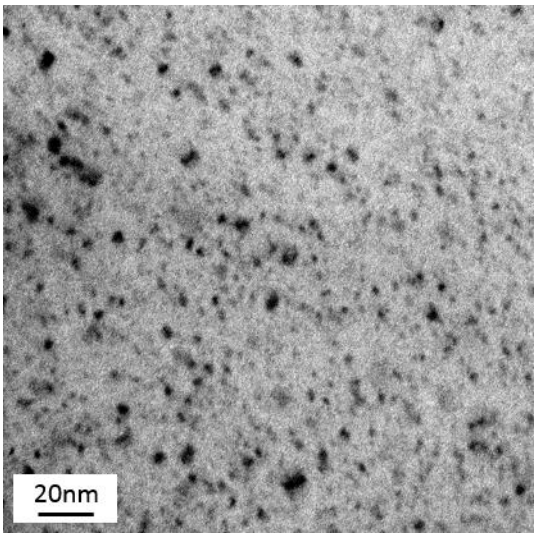

(b). Fast heating to 350°C +water quenching

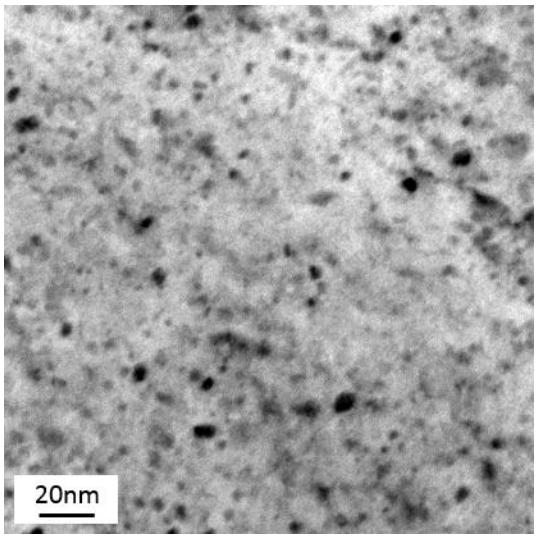

(c). Fast heating to 450°C +water quenching

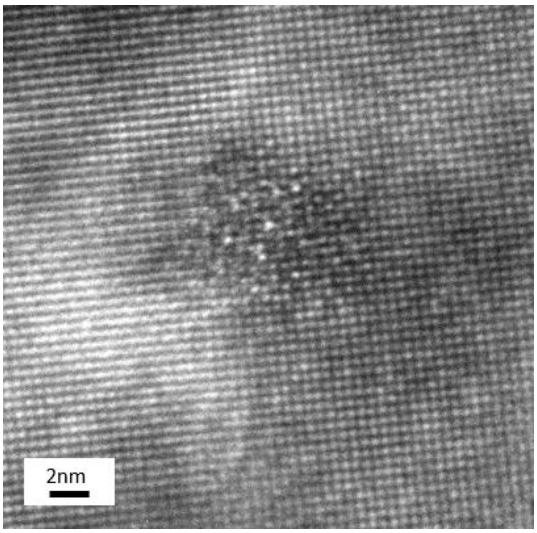

(d). HR-TEM of the pre-β'' precipitates

Fig. 4. TEM bright field images of microstructures observed in the <100> Al zone axis orientation after fast heating and water quenching

It is well accepted that the Mg/Si ratio of pre-β" is over 1, their shape is almost spherical with approximately 3nm radius and these precipitates are well coherent with the matrix, which is consistent with the observed precipitates above (Marioara et al., 2003). Regarding the morphology and the ratio of Mg to Si, these dot-like precipitates are identified to be pre-*β"* phase. All meta-stable clusters of the raw material (T4 temper) are dissolved again in the matrix during ultra-fast heating. As the cooling rate of water quenching (greater than 1000°C/s) is far higher than the required critical quenching rate, the increased post-quenched hardness is attributed to the formation of these pre-*β"* precipitates in the heating process (heated to 300, 350 and 450°C) instead of the cooling process (Milkereit et al., 2012; Zhang et al., 2018). In the case of continuous fast heating to 450°C, most of the formed precipitates may have dissolved into the matrix resulting in an infinitesimal amount remaining, which corresponds with the precipitate number density observed in TEM images. This results in the initial hardness of curve (a) being the lowest of the three (56.9HV) although still greater than the as-quenched value (48HV). Growth and coarsening of precipitates occurs quickly compared to the material in SSSS state because these pre-*β"* precipitates consume solute elements and quenched-in vacancies and readily transfer to the strongest needle-shaped *β"* precipitates in the artificial ageing. More solute atoms will accumulate around these precipitates as less diffusion energy is needed.

The size and volume fraction of the pre-existing precipitates are specified and would be implemented in the age-hardening sub model as the initial material condition. The evolutions of these precipitates are tracked in the subsequent computation to accurately predict the overall strength.

4.2 Effect of residual dislocations on the post-form strength

Different samples were generated to investigate the effect of residual dislocations on precipitation response, as illustrated in Table 3.

Table 3. Peak hardness and the corresponding ageing time for the samples with different pre-strained conditions (ageing at 180°C)

Strain rate (s^{-1})	Strain	Post-quenched hardness (HV)	Peak hardness (HV)	Peak ageing time (h)
0	0	48.0	122.2	6
0.01	10%	56.1	118.3	3.5
0.1	10%	58.9	119.0	3.25
1	10%	63.8	121.3	3
1	30%	65.8	120.9	2.5

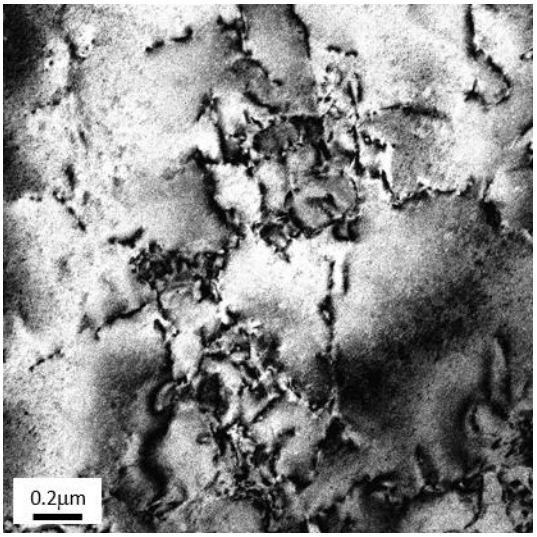

a. As-quenched sample with pre-strain (10%)

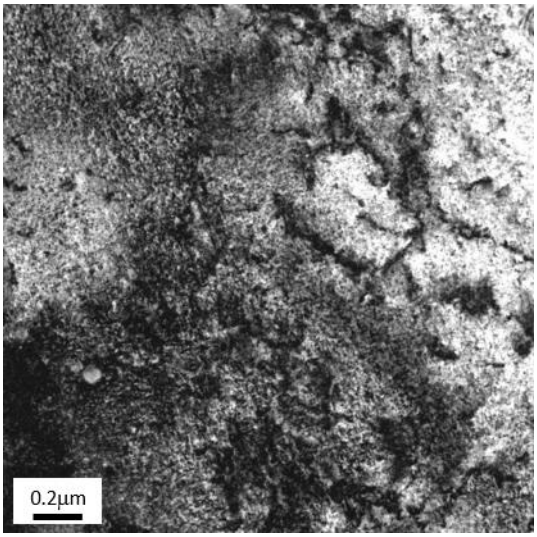

b. Under-aged sample with pre-strain (10%)

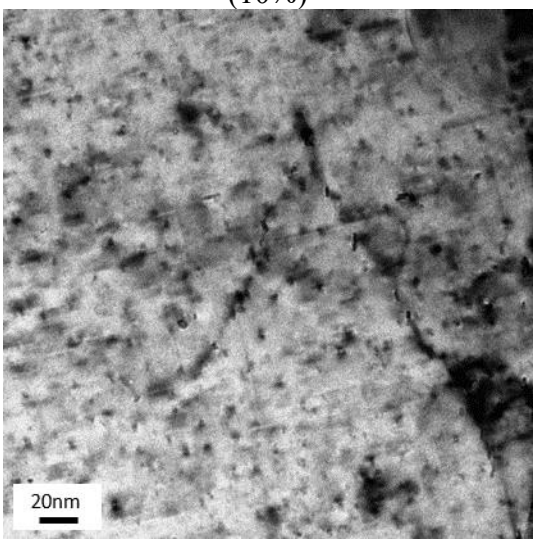

c. Under-aged sample with pre-strain (180°C)

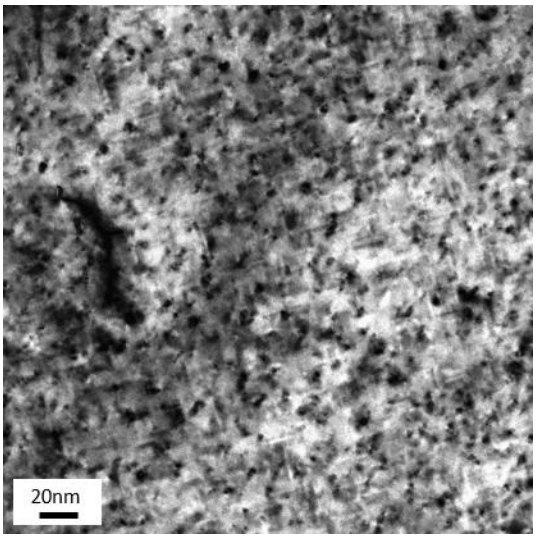

d. Peak-aged sample with pre-strain (180°C)

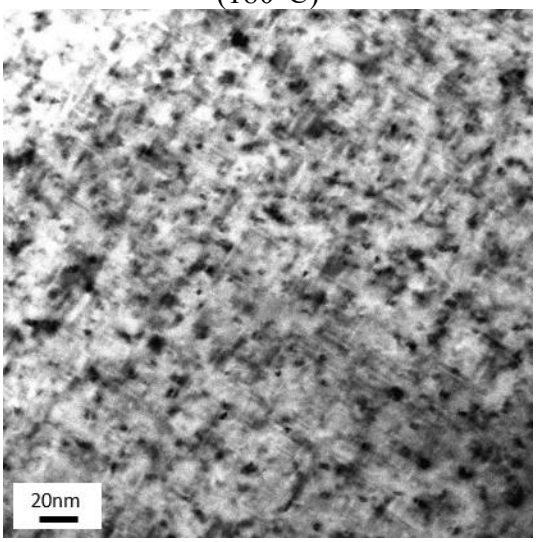

e. Peak-aged sample without pre-strain (180°C)

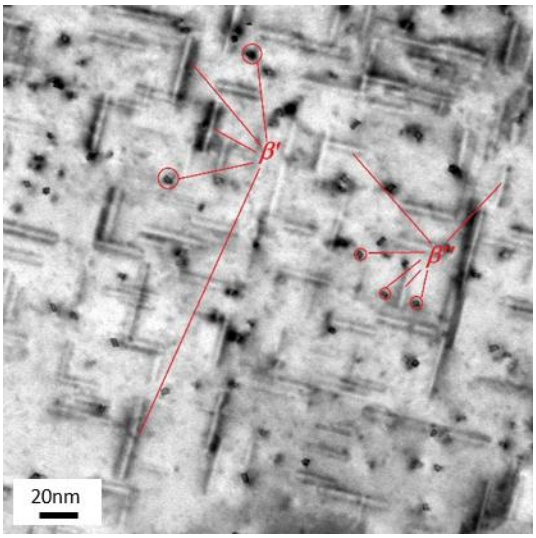

f. Peak-aged sample without pre-strain (220°C)

Fig. 5. TEM bright field images of microstructures observed in the <100> Al zone axis orientation after artificial ageing with/without pre-strain

TEM analysis was conducted on a pre-strained specimen without ageing and multiple specimens that had been aged at 180 or 220°C with/without pre-strain as shown in Fig. 5. Two major types of precipitates (needle-shaped *β''* and rod-shaped *β'* morphology), aligned along the <100> major axis of aluminium matrix were observed in the workpieces experienced various ageing procedures. The needle-shaped precipitates were identified based on their tiny regular quadrilateral end-on views while rod-shaped precipitates were recognized according to their large cross sectional view and long elongated rod shapes.

Fig. 5 (a) demonstrates large numbers of residual dislocations observed in the as-quenched specimen. It is noticed from Fig. 5 (b) that the density of dislocations decreases as artificial ageing begins. Figs. 5 (c) and (d) show the bright-field TEM micrographs of pre-strained specimens aged at 180°C for 1h and 3h, respectively. Small *β''* precipitates (approximately 12.4nm in length) are the dominant microstructural phases in Fig. 5 (c) and a large number of dislocations are observed in the grains. In Fig. 5 (d), the dislocation density is decreased and the needle-shaped *β''* phase precipitates grow gradually from 12.4nm to around 15.6nm. Moreover, some rod-shaped *β'* precipitates also exist. Figs. 5 (e) and (f) show the typical micrographs of the un-deformed specimens peak-aged at 180°C and 220°C, where *β''* and *β'* phase precipitates can be observed. The needle-shaped *β''* and rod-shaped *β'* can be differentiated based on their respective shape of cross sections. The cross section of highly coherent *β''* follows the rectangular or parallelogram shape when scanned along <100> axis, matching the arrangement of a monoclinic unit cell identified earlier (Marioara et al., 2006). The *β'* precipitates clearly appear larger and have more roundish and irregular cross sections (Du et al., 2016). In addition, the average size of precipitates in Fig. 5 (e) is evidently smaller than in Fig. 5(f) (13.2nm vs 28.8nm in length).

During the high temperature tensile tests, all the T4 temper specimens were pre-stretched (10% and 30%) with different strain rates (0.01, 0.1 and $1s^{-1}$) prior to artificial ageing. It is deduced from the post-quenched hardness in Table 2 that a higher strain rate and amount of pre-strain at deformation period would induce larger dislocation densities but remain even after water quenching. The presence of these residual dislocations will strongly influence the mechanical properties of the aluminium alloys, especially strength. In the hot/warm stamping process, the dislocation density in a material increases with plastic deformation, following the relationship: $\rho \propto \tau^2$, where τ is flow stress and ρ is dislocation density (Dieter and Bacon, 1986; He et al., 2016). According to the Frank-Read theory, these dislocations frequently propagate and pile up on slip planes at the grain boundaries (Huang et al., 2014). On the other hand, in high temperature deformation, dislocations become mobile and are able to glide, cross-slip and climb, where annihilation of dislocations becomes possible (Pei and Stocks, 2018; Yan et al., 2016). The residual dislocations are dependent on the amount of strain and strain rate due to different recovery times at high temperature. The tangled dislocations gradually increase the resistance to further dislocation motion, and hence strengthen the material (Krasnikov and Mayer, 2018; Záležák et al., 2017). This strain hardening effect explains the higher hardness of specimens after pre-straining when compared to the SSSS specimen. After water quenching, dislocations act as sinks for quenched-in vacancies so that the suppressed supersaturated state of the aluminium matrix prevents low-temperature clustering activities (Birol, 2005c). These clusters otherwise have a detrimental effect on the precipitation response of the material, because they are difficult to dissolve and are not

suitable nucleation sites for the main hardening phase *β''* (Martinsen et al., 2012; Torster et al., 2010). On the contrary, dislocations act as favourable nucleation sites for the pre-*β''* phase precipitates. The slower bulk diffusion mechanism for the formation of precipitates is replaced by the faster dislocation-assisted diffusion mechanism (Kolar et al., 2012). The presence of dislocations ensures more solute elements but also a larger driving force to form GP-I zones that readily grow to *β''* phase, following the artificial ageing process. In the early stage of artificial ageing, the density of the precipitates is higher and the distribution of the precipitates is evenly dispersed for the pre-strained specimen, contributing to a shorter required time to obtain peak hardness compared with the non-deformed specimen. As seen in Figs. 6 (c) and (d), numerous precipitates are distributed around the dislocations in the pre-deformed specimens. As ageing continues, however, the drawbacks associated with induced dislocations are observed. Due to the faster growth and coarsening rates provided from dislocations, the hardening *β''* phase and rod-shaped *β'* phase precipitates in the pre-deformed specimen begin to coarsen earlier as compared to the non-deformed specimen. This can be observed from the precipitate sizes in Figs. 6 (d) and (e) (15.6nm vs 12.4nm in length). Consequently, the peak hardness of pre-strained specimens is lower than that of non-deformed specimens. Moreover, the precipitates coarsen more rapidly under higher ageing temperature as observed in Figs. 6 (e) and (f).

In conclusion, the presence of induced dislocations influences the change of strength of the material significantly. The strain hardening and accelerating effects are beneficial while the loss of peak strength can also occur, which depends on the pre-strain levels.

4.3 Effect of multi-stage artificial ageing on the post-form strength

The effect of multi-stage artificial ageing parameters on the measured post-form strength is shown in Table 4. The first-stage ageing was conducted at 220°C with the time ranging from 3 to 6 minutes and the second-stage ageing was then carried out at 190°C for 20, 40, 120 and 240 minutes to determine the ageing response on hardness values.

Table 4. Hardness of the specimen during two-stage artificial ageing (Unit: HV)

1st stage 220°C ageing time (min)	2nd stage 190°C ageing time (min)			
	20	40	120	240
3	101.9	111.0	116.3	113.7
4	103.2	110.7	114.6	113.8
5	101.9	109.2	114.0	110.8
6	99.6	98.7	112.3	111.3

Importantly, the peak hardness of one-stage ageing at 190 and 220°C are 118.0 and 107.7HV respectively. For the two-stage ageing results shown in Table 3, all of the peak values of the two-stage ageing lie between 118.0 and 107.7HV and the peak strength decreases with the increase of ageing time at 220°C.

This phenomenon can be explained by the effect of temperature on the ageing response of the Al-Mg-Si alloys. Theoretically, the equilibrium solute concentration at lower ageing temperature is less than that of higher temperature due to the reduced matrix phase solubilities. The volume fraction is directly proportional to the loss of solute concentration in aluminium matrix. Therefore, the equilibrium volume fraction of precipitates decreases with

the increasing ageing temperature, indicating that fewer precipitates form at higher temperature. Furthermore, the higher ageing temperature accelerates the formation, growth and coarsening of precipitates due to the faster solute transportation via diffusion. Given that precipitation hardening is the controlling hardening mechanism during ageing, the fewer formed equilibrium precipitates and the coarser distribution of precipitates inversely affect the hardness, leading to a lower peak hardness. The distribution of precipitates formed at the first-stage ageing (220°C) is non-uniform in nature. However, during the second-stage ageing (190°C), the remaining alloying elements can precipitate around the nucleation sites more finely and uniformly, which cancel out the effect of the first-stage ageing to a certain extent. This results in the peak strength of two-stage ageing being greater than one-stage ageing (at 220°C) and lower than that with 190°C ageing.

4.4 Calibration of the unified post-form strength prediction model

The values of the parameters used in both viscoplastic deformation model and artificial ageing model are shown in Tables 5 and 6. Each parameter represents a physical characteristic of the material and was determined based on the parameter boundary conditions presented in the literature (Lin and Liu, 2003; O R Myhr et al., 2001; Shercliff and Ashby, 1990; A. Wang et al., 2017) and optimised via Simulated Annealing (SA) algorithm. The detailed methodology to obtain them is illustrated in the Appendix.

Table 5. Materials parameters of the viscoplastic deformation model

E(MPa)	k(MPa)	K(MPa)	n_1	A_0	B(MPa)	C_p	n_2
35000	0.05	42.5	7	18	6	8.5	5

Table 6. Materials parameters of the artificial ageing model

R (J/mol K)	σ_i (HV)	Q_A (kJ/mol K)	T_s (K)	Q_s (kJ/mol K)	k_1	C_1	C_2
8.314	15	140	553	25	0.5	0.00045	380
C_3	C_4	f_{max}	C_s	C_i	n_2	A_d	C_{ageing}
635632	0.0450	0.00695	0.0263	0.025	35000	0.05	42.5
B_1	B_2						
7.8E-07	1.5E-13						

Fig. 6 (a) and (b) show the stress-strain curves of AA6082 deformed at a constant temperature with different strain rates and a constant strain rate with varying temperatures, respectively. The symbols in the figure represent the experimental data and the solid line refers to the modelling results. The modelling results fit very well with the experimental ones for all three strain rates within the acceptable accuracy. Crucially, the general trend of flow stress is increased with strain rate due to strain hardening and strain rate hardening, which is captured well by the model.

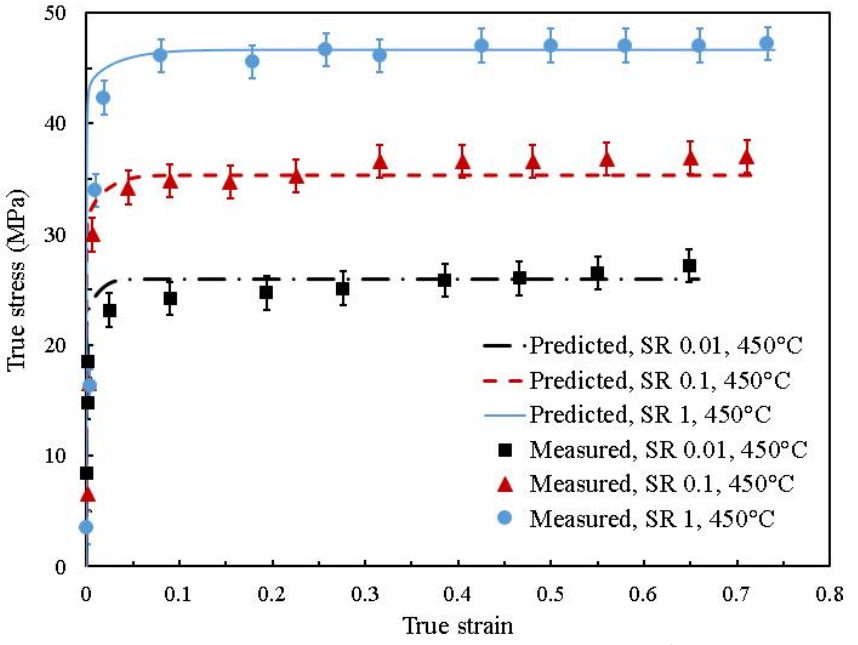

a. 450°C, strain rates 0.01, 0.1, 1s^{-1}

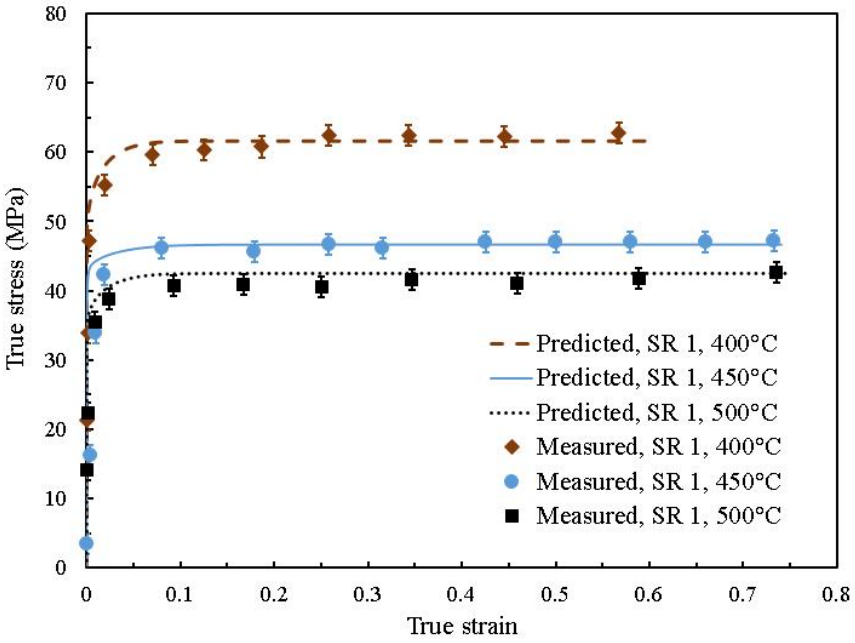

b. SR 1s^{-1}, temperatures 400, 450, 500ºC

Fig. 6. The measured and modelled stress-strain curves of AA6082 at different strain rates and temperatures

Furthermore, the comparison between the experimented and modelled hardness values for the ageing at different temperatures without pre-strain are given in Fig. 7. It can be clearly seen that the model captures the general trend and the peak hardness values with a deviation of less than 5%. The best fit can be observed for the 180°C curve and this is advantageous as this temperature yields the most optimum value of the post-form strength. The complex effects of temperature during artificial ageing on the interdependent evolutions of microstructural variables, such as solute concentration, volume fraction of precipitates, and average radius of precipitates, were determined with an excellent detail and precision.

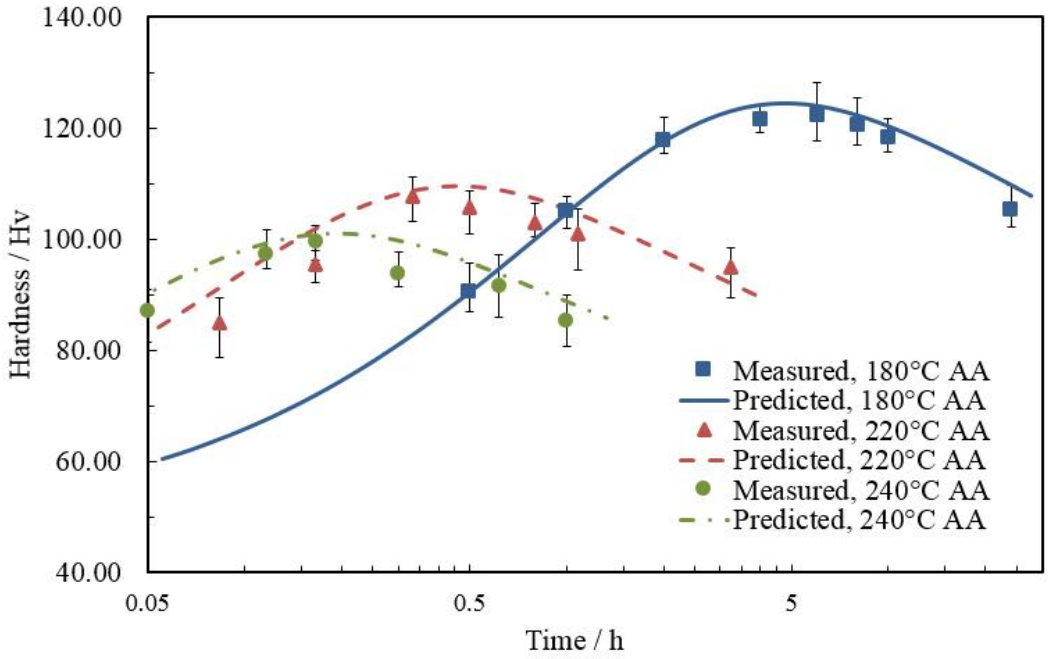

Fig. 7. Comparison between the experimental results and model predicted hardness for the specimen aged at different temperatures

Fig. 8 illustrates the comparisons between the experimental and modelled hardness values for ageing at 180°C with different heating target temperatures. This ageing temperature value was chosen as it gave the highest strength and the best model fit in Fig. 7. The evolutions of the normalized volume fraction of precipitates, $\overline{f}$, is displayed in Fig. 10. All three curves of f increase sharply in the early stages of ageing, slowing in the latter stages and eventually levelling out to 1 at the end of ageing. The normalized volume fraction of the specimen heated to 350°C is greater than that of the ones heated to 300 and 450°C in the earlier stages of ageing. The results are consistent with the proposed theory in Section 3.1 and are thus verified by TEM and hardness measurements.

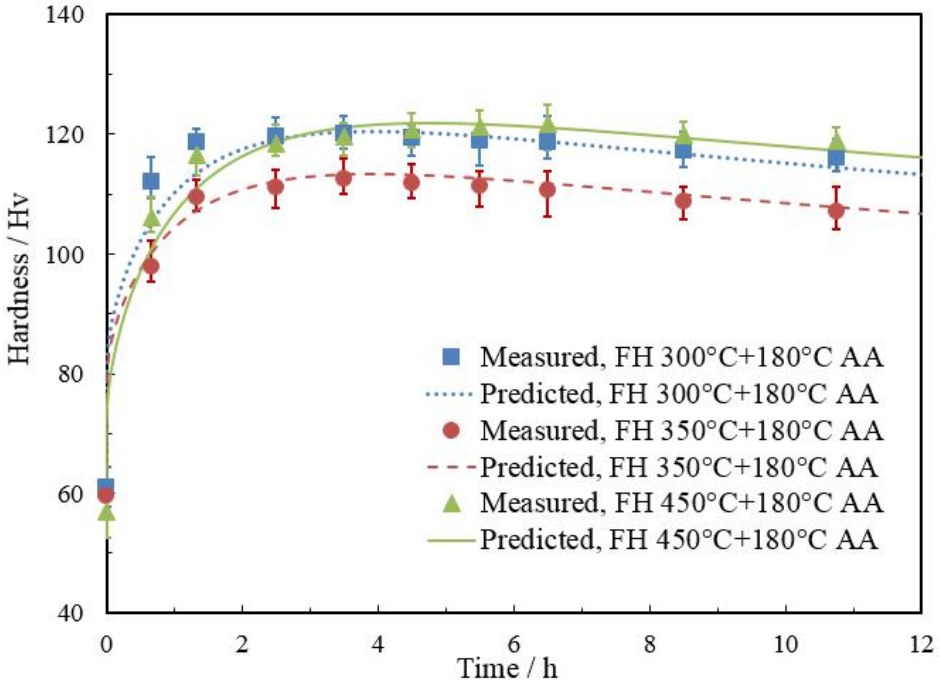

Fig. 8. Comparison between the experimental results and the modelled hardness for the specimen aged at 180°C ageing with different target heating temperatures.

The hardness evolutions for ageing at 180°C with different amounts of pre-strain and strain rates are shown in Fig. 9. As shown in the figure, a good agreement between the modelled results and experimental ones is obtained with the majority of the modelled curves (produced by using the equations in Section 2.2) within the error bars of the experiments. The difference between the post-form strength prediction model and the experimental data is less than 5%, and accurately captures the hardness evolution during the artificial ageing process. Furthermore, the hardness for the pre-strained workpieces increases steeply during the early stage ageing and drops more rapidly than that of the undeformed workpieces. This is because the induced dislocations accelerate the artificial ageing response.

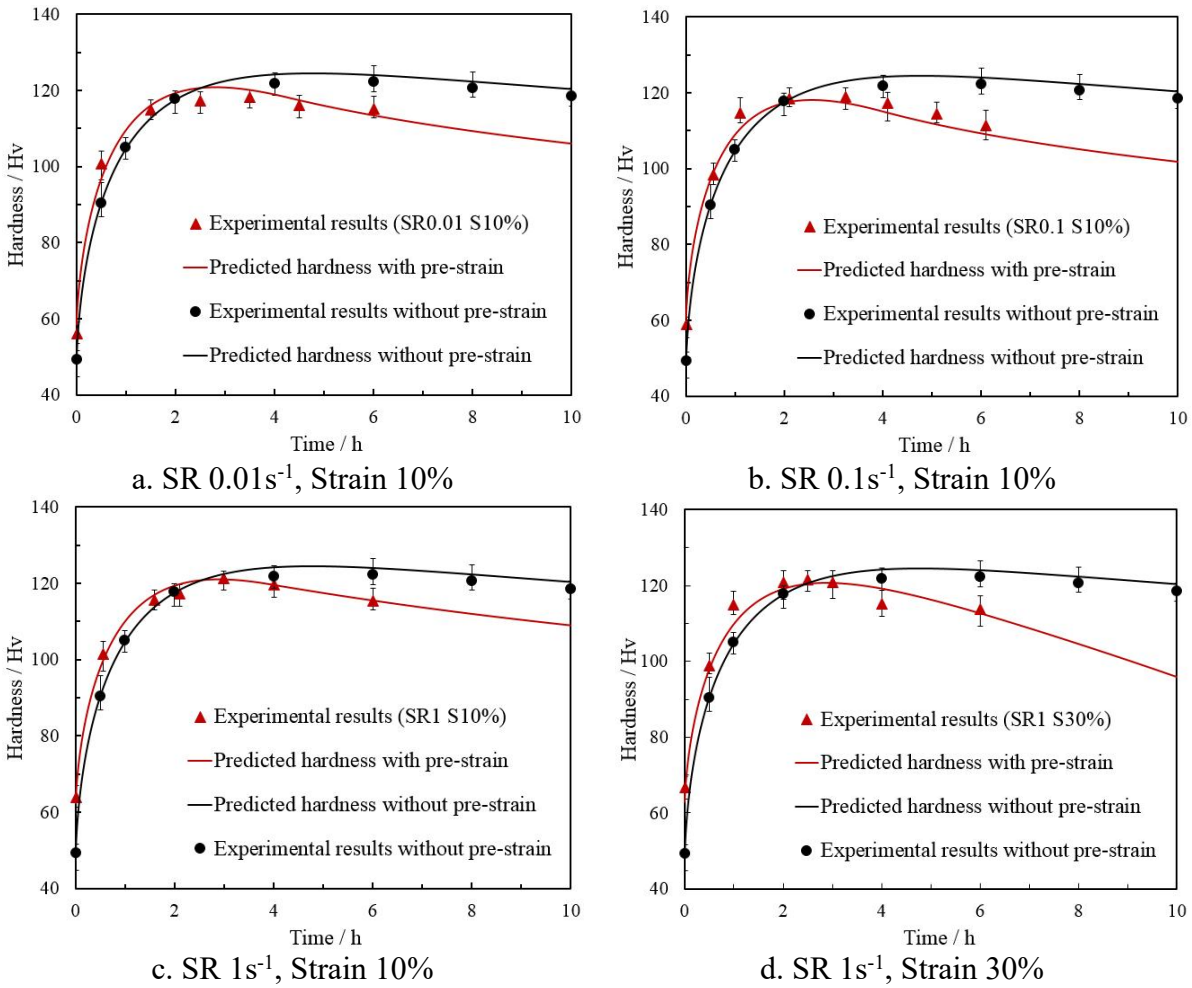

a. SR 0.01s^{-1}, Strain 10%

b. SR 0.1s^{-1}, Strain 10%

c. SR 1s^{-1}, Strain 10%

d. SR 1s^{-1}, Strain 30%

Fig. 9. Comparison between the experimental results and the modelling of hardness evolution for the specimen with different amounts of pre-strain and strain rate

The comparative results of the multi-stage artificial ageing are shown in Fig. 10. While the first stage ageing lies slightly outside the error bar region of the experiment, the majority of the second stage ageing is within the region. This confirms that the model is capable of modelling complex two-stage ageing phenomenon, at different temperatures, and handles the

evolving microstructures. Another extension would be to model further and more advanced ageing routines to investigate the restrictions of the current model.

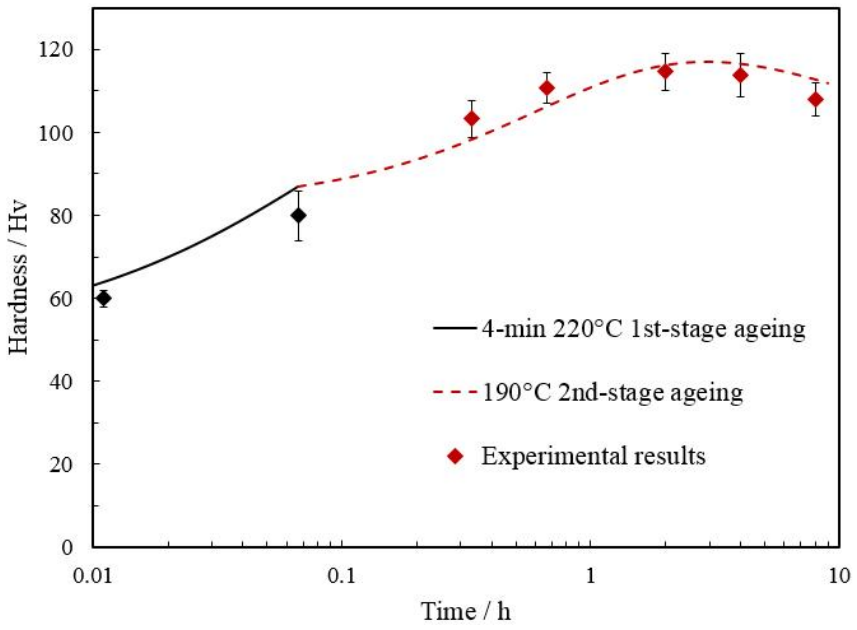

Fig. 10. Comparison between the experimental and the modelled hardness evolution for the specimen after two-stage ageing

4.5 Validation of the unified post-form strength prediction model

In order to independently validate the model, the model was applied to an experimentally formed AA6082 component, of which the blank was in T4 temper. The U-shaped workpiece was formed successfully via Uni-Form.

Fig. 11 demonstrates the simulated hardness evolution of the half U-shaped component during artificial ageing at 180°C after ultra-fast heating and hot/warm stamping. The ageing times range from 0 to 4h until the peak hardness of the overall workpiece is obtained. The predicted and measured hardness distribution for a U-shaped component after 2-hour and 4-hour artificial ageing at 180°C is shown in the left half of Fig. 12, with the upper right showing the real stamped component. The stamped U-shape is marked with locations 1, 2 and 3, which were used to measure hardness and validate the model. Specifically, location 1 lies in the centre of the bottom surface, location 2 is at the corner of the bottom surface and location 3 stands for the centre of the side wall. These specific locations were chosen to provide the representative results in the typical failure-prone areas of the whole component.

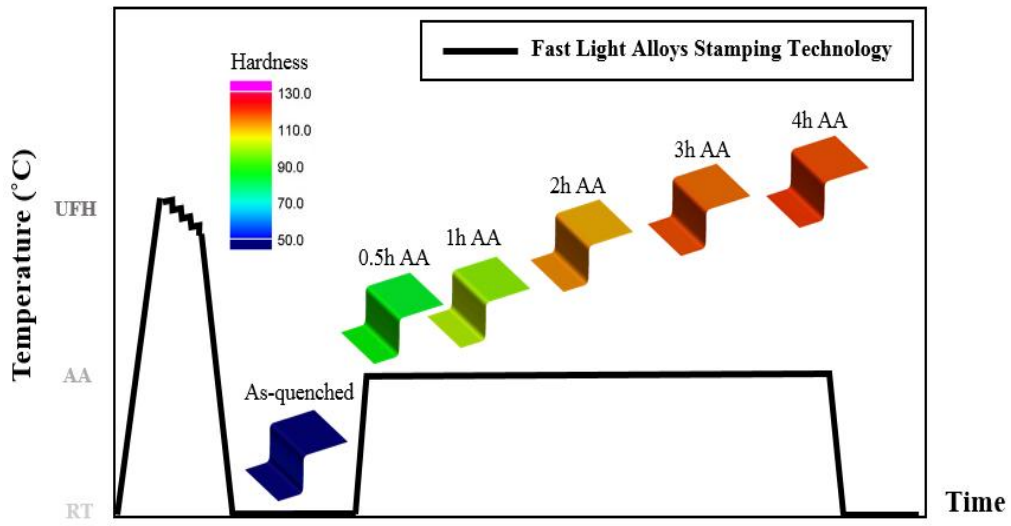

Fig. 11. Simulated hardness evolution for the U-shaped workpiece undergoing Ultra-fast heating & Hot stamping & AA

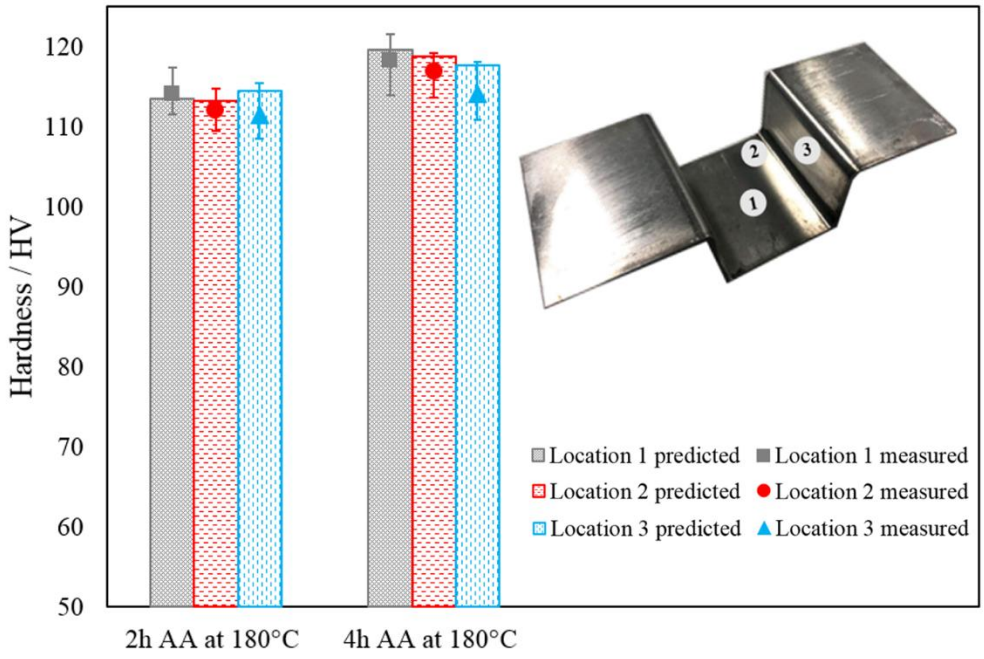

Fig. 12. Comparison between experiments and modelled hardness for the U-shaped workpiece

A good agreement for all the locations has been achieved and the predicted hardness values are within the error bars. The error bars for location 3 are slightly larger than the other two locations after both 2-h artificial ageing and 4-h artificial ageing. A possible reason is that the quenching rate of side wall is slightly lower due to the lack of holding force from the dies. As can be seen, hardness of most regions is approximately 118HV, which meets the T6 requirements. In general, the deviation between modelled results and experimental data is less than 5%, which proves that the unified constitutive model is sufficiently robust and accurate to predict post-form strength of 6xxx series aluminium alloys in the real manufacturing process.

5. Conclusions

In the present research, a series of systematic experiments involving EDXS, TEM analyses, tensile tests and hardness measurements were conducted. The aim was to investigate the effects of precipitates and dislocations on age hardening behaviour and a post-form strength prediction (PFS) model was proposed. The mechanical behaviour during hot/warm stamping as well as precipitation hardening responses in the subsequent multi-stage artificial ageing treatment was simulated. The following conclusions can be drawn:

1. A post-form strength prediction (PFS) model was established based on the intricate correlations of the important microstructural variables including dislocation density, solute concentration, volume fraction and average radius of precipitates. The PFS model was successfully validated by experimental data and a hot stamped U-shaped component was treated with subsequent multi-stage artificial ageing. The maximum error is less than 5%.

2. Under ultra-fast heating conditions, it was found that dot-like precipitates with the mean radius of approximately 3.9nm were finely dispersed in the aluminium matrix of AA6082. These spherical precipitates are suggested to be pre-β'' phase precipitates. These pre-existing precipitates are readily transferred to the major hardening needle-shaped β'' precipitates, leading to reduced time as artificial ageing proceeds.

3. The residual dislocations induced during the high temperature plastic deformation alter the precipitation response of 6xxx series aluminium alloys in several ways. They strengthen the material and act as nucleation sites for pre-β'' phase precipitates, which favours the formation of β'' phase precipitates and hence accelerates the precipitation process. On the other hand, the formed precipitates tend to accumulate around the dislocations in the subsequent artificial ageing, leading to the coarser distribution of precipitates and loss of peak strength as well.

This research provides insights into microstructural changes during ultra-fast heating, hot/warm stamping and multi-stage artificial ageing. The proposed PFS model is a powerful tool for understanding the complicated thermo-mechanical processes and optimising the processing windows for manufacturing of complicated parts made of high strength aluminium alloys. Furthermore, the modelling framework and methodology proposed in this research could be used as a useful protocol to analyse and optimise hot/warm stamping processes of other alloys.

References

Allwood, J.M., Shouler, D.R., 2009. Generalised forming limit diagrams showing increased forming limits with non-planar stress states. Int. J. Plast. 25, 1207–1230. https://doi.org/10.1016/j.ijplas.2008.11.001

Birol, Y., 2005a. Pre-straining to improve the bake hardening response of a twin-roll cast Al-Mg-Si alloy. Scr. Mater. 52, 169–173. https://doi.org/10.1016/j.scriptamat.2004.10.001

Birol, Y., 2005b. Pre-straining to improve the bake hardening response of a twin-roll cast Al–Mg–Si alloy. Scr. Mater. 52, 169–173.

Birol, Y., 2005c. Pre-aging to improve bake hardening in a twin-roll cast Al – Mg – Si alloy. Mater. Sci. Eng. A 391, 175–180. https://doi.org/10.1016/j.msea.2004.08.069

Csanádi, T., Chinh, N.Q., Gubicza, J., Vörös, G., Langdon, T.G., 2014. Characterization of stress-strain relationships in Al over a wide range of testing temperatures. Int. J. Plast. 54, 178–192. https://doi.org/10.1016/j.ijplas.2013.08.014

Deschamps, A., Brechet, Y., 1999. Influence of predeformation and ageing of an Al-Zn-Mg alloy-II. Modeling of precipitation kinetics and yield stress. Acta Mater. 47.

Dieter, G.E., Bacon, D.J., 1986. Mechanical metallurgy. McGraw-hill New York.

Du, Q., Holmedal, B., Friis, J., Marioara, C.D., 2016. Precipitation of Non-spherical Particles in Aluminum Alloys Part II : Numerical Simulation and Experimental Characterization During Aging Treatment of an Al-Mg-Si Alloy. Metall. Mater. Trans. A 47, 589–599. https://doi.org/10.1007/s11661-015-3196-6

Du, Q., Tang, K., Marioara, C.D., Andersen, S.J., Holmedal, B., Holmestad, R., 2017. Modeling over-ageing in Al-Mg-Si alloys by a multi-phase CALPHAD-coupled Kampmann-Wagner Numerical model. Acta Mater. 122, 178–186. https://doi.org/10.1016/j.actamat.2016.09.052

Engels, P., Ma, A., Hartmaier, A., 2012. Continuum simulation of the evolution of dislocation densities during nanoindentation. Int. J. Plast. 38, 159–169. https://doi.org/10.1016/j.ijplas.2012.05.010

Esmaeili, S., Lloyd, D.J., Poole, W.J., 2005. Modeling of precipitation hardening in pre-aged AlMgSi(Cu) alloys. Acta Mater. 53, 5257–5271. https://doi.org/10.1016/j.actamat.2005.08.006

Esmaeili, S., Lloyd, D.J., Poole, W.J., 2003a. Modeling of precipitation hardening for the naturally aged Al-Mg-Si-Cu alloy AA6111. Acta Mater. 51, 3467–3481. https://doi.org/10.1016/S1359-6454(03)00167-8

Esmaeili, S., Lloyd, D.J., Poole, W.J., 2003b. A yield strength model for the Al-Mg-Si-Cu alloy AA6111. Acta Mater. 51, 2243–2257. https://doi.org/10.1016/S1359-6454(03)00028-4

Garrett, R.P., Lin, J., Dean, T.A., 2005. An investigation of the effects of solution heat treatment on mechanical properties for AA 6xxx alloys: experimentation and modelling. Int. J. Plast. 21, 1640–1657.

Gracio, J.J., Barlat, F., Rauch, E.F., Jones, P.T., Neto, V.F., Lopes, A.B., 2004. Artificial aging and shear deformation behaviour of 6022 aluminium alloy. Int. J. Plast. 20, 427–445. https://doi.org/10.1016/S0749-6419(03)00095-0

He, B.B., Luo, H.W., Huang, M.X., 2016. Experimental investigation on a novel medium Mn steel combining transformation-induced plasticity and twinning-induced plasticity effects. Int. J. Plast. 78, 173–186. https://doi.org/10.1016/j.ijplas.2015.11.004

Holmedal, B., Osmundsen, E., Du, Q., 2016. Precipitation of Non-Spherical Particles in Aluminum Alloys Part I : Generalization of the Kampmann – Wagner Numerical Model. Metall. Mater. Trans. A 47. https://doi.org/10.1007/s11661-015-3197-5

Hu, Q., Zhang, L., Ouyang, Q., Li, X., Zhu, X., Chen, J., 2018. Prediction of forming limits for anisotropic materials with nonlinear strain paths by an instability approach. Int. J. Plast. 103, 143–167. https://doi.org/10.1016/j.ijplas.2018.01.006

Huang, M., Li, Z., Tong, J., 2014. The influence of dislocation climb on the mechanical behavior of polycrystals and grain size effect at elevated temperature. Int. J. Plast. 61, 112–127. https://doi.org/10.1016/j.ijplas.2014.06.002

Kabirian, F., Khan, A.S., Gnäupel-Herlod, T., 2015. Visco-plastic modeling of mechanical responses and texture evolution in extruded AZ31 magnesium alloy for various loading conditions. Int. J. Plast. 68, 1–20. https://doi.org/10.1016/j.ijplas.2014.10.012

Kampmann, R., Eckerlebe, H., Wagner, R., 1985. Precipitation Kinetics in Metastable Solid Solutions – Theoretical Considerations and Application to Cu-Ti Alloys. MRS Proc. 57, 525. https://doi.org/10.1557/PROC-57-525
Khan, A.S., Kazmi, R., Pandey, A., Stoughton, T., 2009. Evolution of subsequent yield surfaces and elastic constants with finite plastic deformation. Part-I: A very low work hardening aluminum alloy (Al6061-T6511). Int. J. Plast. 25, 1611–1625. https://doi.org/10.1016/j.ijplas.2008.07.003
Khan, A.S., Pandey, A., Stoughton, T., 2010. Evolution of subsequent yield surfaces and elastic constants with finite plastic deformation. Part III: Yield surface in tension-tension stress space (Al 6061-T 6511 and annealed 1100 Al). Int. J. Plast. 26, 1421–1431. https://doi.org/10.1016/j.ijplas.2009.07.008
Khan, I.N., Starink, M.J., Yan, J.L., 2008. A model for precipitation kinetics and strengthening in Al-Cu-Mg alloys. Mater. Sci. Eng. A 472, 66–74. https://doi.org/10.1016/j.msea.2007.03.033
Kolar, M., Pedersen, K.O., Gulbrandsen-Dahl, S., Marthinsen, K., 2012. Combined effect of deformation and artificial aging on mechanical properties of Al-Mg-Si Alloy. Trans. Nonferrous Met. Soc. China (English Ed. 22, 1824–1830. https://doi.org/10.1016/S1003-6326(11)61393-9
Kolar, M., Pedersen, K.O., Gulbrandsen-Dahl, S., Teichmann, K., Marthinsen, K., 2011. Effect of Pre-Deformation on Mechanical Response of an Artificially Aged Al-Mg-Si Alloy. Mater. Trans. 52, 1356–1362. https://doi.org/10.2320/matertrans.L-MZ201127
Krasnikov, V.S., Mayer, A.E., 2018. Influence of local stresses on motion of edge dislocation in aluminum. Int. J. Plast. 101, 170–187. https://doi.org/10.1016/j.ijplas.2017.11.002
Li, H., Wu, C., Yang, H., 2013. Crystal plasticity modeling of the dynamic recrystallization of two-phase titanium alloys during isothermal processing. Int. J. Plast. 51, 271–291. https://doi.org/10.1016/j.ijplas.2013.05.001
Lin, J., Liu, Y., 2003. A set of unified constitutive equations for modelling microstructure evolution in hot deformation. J. Mater. Process. Technol. 143, 281–285.
Lin, S.L., Huang, B.H., Chen, F.K., 2014. Strength and formability designs of tube-hydroformed automotive front sub-frame. Procedia Eng. 81, 2198–2204. https://doi.org/10.1016/j.proeng.2014.10.308
Luan, X., Zhang, Q., Fakir, O. El, Wang, L., 2016. Uni-Form : a pilot production line for hot / warm sheet metal forming integrated in a cloud based SMARTFORMING platform. Adv. High Strength Steel Press Hardening 1–5.
Ma, Z., Zhan, L., Liu, C., Xu, L., Xu, Y., Ma, P., Li, J., 2018. Stress-level-dependency and bimodal precipitation behaviors during creep ageing of Al-Cu alloy: Experiments and modeling. Int. J. Plast. 0–1. https://doi.org/10.1016/j.ijplas.2018.07.001
Marioara, C.D., Andersen, S.J., Jansen, J., Zandbergen, H.W., 2003. The influence of temperature and storage time at RT on nucleation of the β ″phase in a 6082 Al–Mg–Si alloy. Acta Mater. 51, 789–796.
Marioara, C.D., Nordmark, H., Andersen, S.J., 2006. Post- β phases and their influence on microstructure and hardness in 6xxx Al-Mg-Si alloys 1, 471–478. https://doi.org/10.1007/s10853-005-2470-1
Martinsen, F.A., Ehlers, F.J.H., Torsæter, M., Holmestad, R., 2012. Reversal of the negative natural aging effect in Al-Mg-Si alloys. Acta Mater. 60, 6091–6101. https://doi.org/10.1016/j.actamat.2012.07.047
Milkereit, B., Wanderka, N., Schick, C., Kessler, O., 2012. Continuous cooling precipitation diagrams of Al-Mg-Si alloys. Mater. Sci. Eng. A 550, 87–96. https://doi.org/10.1016/j.msea.2012.04.033
Myhr, O.R., Grong, O., Andersen, S.J., 2001. Modelling of the age hardening behaviour of Al-Mg-Si alloys. Acta Mater. 49, 65–75. https://doi.org/10.1016/S1359-6454(00)00301-3
Myhr, O.R., Grong, Ø., Andersen, S.J., 2001. Modelling of the age hardening behaviour of Al-Mg-Si Alloys. Acta Mater. 49, 65–75.
Myhr, O.R., Grong, Ø., Fjær, H.G., Marioara, C.D., 2004. Modelling of the microstructure and strength evolution in al-mg-si alloys during multistage thermal processing. Acta Mater. 52, 4997–5008. https://doi.org/10.1016/j.actamat.2004.07.002
Myhr, O.R., Grong, Ø., Pedersen, K.O., 2010. A combined precipitation, yield strength, and work hardening model for Al-Mg-Si alloys. Metall. Mater. Trans. A Phys. Metall. Mater. Sci. 41, 2276–2289. https://doi.org/10.1007/s11661-010-0258-7

Myhr, O.R., Grong, Ø., Schäfer, C., 2015. An extended age-hardening model for Al-Mg-Si alloys incorporating the room-temperature storage and cold deformation process stages. Metall. Mater. Trans. A 46, 6018–6039.
Nieto-Fuentes, J.C., Rittel, D., Osovski, S., 2018. On a dislocation-based constitutive model and dynamic thermomechanical considerations. Int. J. Plast. 108, 55–69. https://doi.org/10.1016/j.ijplas.2018.04.012
Pei, Z., Stocks, G.M., 2018. Origin of the sensitivity in modeling the glide behaviour of dislocations. Int. J. Plast. 106, 48–56. https://doi.org/10.1016/j.ijplas.2018.02.017
Poole, W.J., Shercliff, H.R., Castillo, T., 2013. Process model for two step age hardening of 7475 aluminium alloy 0836. https://doi.org/10.1179/mst.1997.13.11.897
Saito, T., Muraishi, S., Marioara, C.D., Andersen, S.J., Røyset, J., Holmestad, R., 2013. The effects of low Cu additions and predeformation on the precipitation in a 6060 Al-Mg-Si alloy. Metall. Mater. Trans. A 44, 4124–4135.
Shercliff, H.R., Ashby, M.F., 1990. A process model for age hardening of aluminium alloys-I. The model. Acta Metall. Mater. 38, 1789–1802. https://doi.org/10.1016/0956-7151(90)90291-N
Shewmon, P.G., 1963. Diffusion in Solids. McGraw-Hill, New York.
Starink, M.J., Wang, S.C., 2003. A model for the yield strength of overaged Al-Zn-Mg-Cu alloys. Acta Mater. 51, 5131–5150. https://doi.org/10.1016/S1359-6454(03)00363-X
Sun, C.Y., Guo, N., Fu, M.W., Wang, S.W., 2016. Modeling of slip, twinning and transformation induced plastic deformation for TWIP steel based on crystal plasticity. Int. J. Plast. 76, 186–212. https://doi.org/10.1016/j.ijplas.2015.08.003
Torster, M., Hasting, H.S., Lefebvre, W., Marioara, C.D., Walmsley, J.C., Andersen, S.J., Holmestad, R., 2010. The influence of composition and natural aging on clustering during preaging in Al-Mg-Si alloys. J. Appl. Phys. 108. https://doi.org/10.1063/1.3481090
Wang, A., Liu, J., Gao, H., Wang, L.L., Masen, M., 2017. Hot stamping of AA6082 tailor welded blanks: Experiments and knowledge-based cloud – finite element (KBC-FE) simulation. J. Mater. Process. Technol. 250, 228–238. https://doi.org/10.1016/j.jmatprotec.2017.07.025
Wang, L., Sun, Y., Ji, K., Luan, X., El Fakir, O., Cai, Z., Liu, X., 2017. Fast warm stamping of ultra-high strength steel sheets.
Xiao, Y., Chen, J., Cao, J., 2012. A generalized thermodynamic approach for modeling nonlinear hardening behaviors. Int. J. Plast. 38, 102–122. https://doi.org/10.1016/j.ijplas.2012.05.004
Yan, S., Yang, H., Li, H., Yao, X., 2016. A unified model for coupling constitutive behavior and micro-defects evolution of aluminum alloys under high-strain-rate deformation. Int. J. Plast. 85, 203–229. https://doi.org/10.1016/j.ijplas.2016.07.011
Yin, D., Xiao, Q., Chen, Y., Liu, H., Yi, D., Wang, B., Pan, S., 2016. Effect of natural ageing and pre-straining on the hardening behaviour and microstructural response during artificial ageing of an Al-Mg-Si-Cu alloy. Mater. Des. 95, 329–339. https://doi.org/10.1016/j.matdes.2016.01.119
Záležák, T., Svoboda, J., Dlouhý, A., 2017. High temperature dislocation processes in precipitation hardened crystals investigated by a 3D discrete dislocation dynamics. Int. J. Plast. 97, 1–23. https://doi.org/10.1016/j.ijplas.2017.04.017
Zhan, L., Lin, J., Dean, T.A., Huang, M., 2011. Experimental studies and constitutive modelling of the hardening of aluminium alloy 7055 under creep age forming conditions. Int. J. Mech. Sci. 53, 595–605. https://doi.org/10.1016/j.ijmecsci.2011.05.006
Zhang, J., Deng, Y., Zhang, X., 2013. Constitutive modeling for creep age forming of heat-treatable strengthening aluminum alloys containing plate or rod shaped precipitates. Mater. Sci. Eng. A 563, 8–15. https://doi.org/10.1016/j.msea.2012.10.055
Zhang, Q., Luan, X., Dhawan, S., Politis, D.J., Cai, Z., 2018. Investigating the quench sensitivity of high strength AA6082 aluminium alloy during the new FAST forming process. IOP Conf. Ser. Mater. Sci. Eng. 418ó. https://doi.org/10.1088/1757-899X/418/1/012028
Zhang, Y., Ngan, A.H.W., 2018. Dislocation-density dynamics for modeling the cores and Peierls stress of curved dislocations. Int. J. Plast. 104, 1–22. https://doi.org/10.1016/j.ijplas.2018.01.009
Zheng, J.H., Lin, J., Lee, J., Pan, R., Li, C., Davies, C.M., 2018. A novel constitutive model for multi-step stress relaxation ageing of a pre-strained 7xxx series alloy. Int. J. Plast. 106, 31–47. https://doi.org/10.1016/j.ijplas.2018.02.008

Nomenclatures

Variables or constants	Specification
σ_{total}, σ_{dis}, σ_y, σ_{ss}, σ_i, σ_{ppt}, σ_{by}, σ_{sh}	Flow stress, dislocation hardening strength, yield stress, solid solution strength, intrinsic strength of aluminium matrix, strength of precipitates, strength of bypassing precipitates, strength of shearable precipitates
E	Young's modulus
ε_T, ε_p	Total strain, plastic strain
$n_1, n_2, A_0, A_d, B, C_p, k, K, \alpha$	Material constants in the viscoplastic deformation sub-model
ρ, ρ_i, ρ_m, $\overline{\rho}$	Dislocation density, initial dislocation density, maximum dislocation density, normalized dislocation density
M	Taylor factor
G	Shear modulus
b	Burgers vector
C_e, C_s, C_t, C_i, C_0, C_{pep}, C_x	Equilibrium solute concentration, maximum solute concentration, transient solute concentration, initial solute concentration, solute concentration at SSSS, loss of solute concentration due to pre-existing precipitates and solute concentration after first-stage ageing
R	Universal gas constant
T, T_s	Temperature, solvus temperature
Q_s, Q_A	Solvus boundary enthalpy, Activation energy for volume diffusion of atoms
$\tau, k_1, B_1, B_2, C_{ageing}$ C_1, C_2, C_3, C_4	Material constants for artificial ageing sub-model
$t, t_p, t_{eq,c}, t_{eq,r}$	Artificial ageing time, time to achieve peak strength
f_t, f_e, f_{max}, f_x	Transient volume fraction, equilibrium volume fraction, maximum volume fraction and volume fraction after first-stage ageing of precipitates
r, r_0	Average radius and initial average radius of precipitates

Appendix

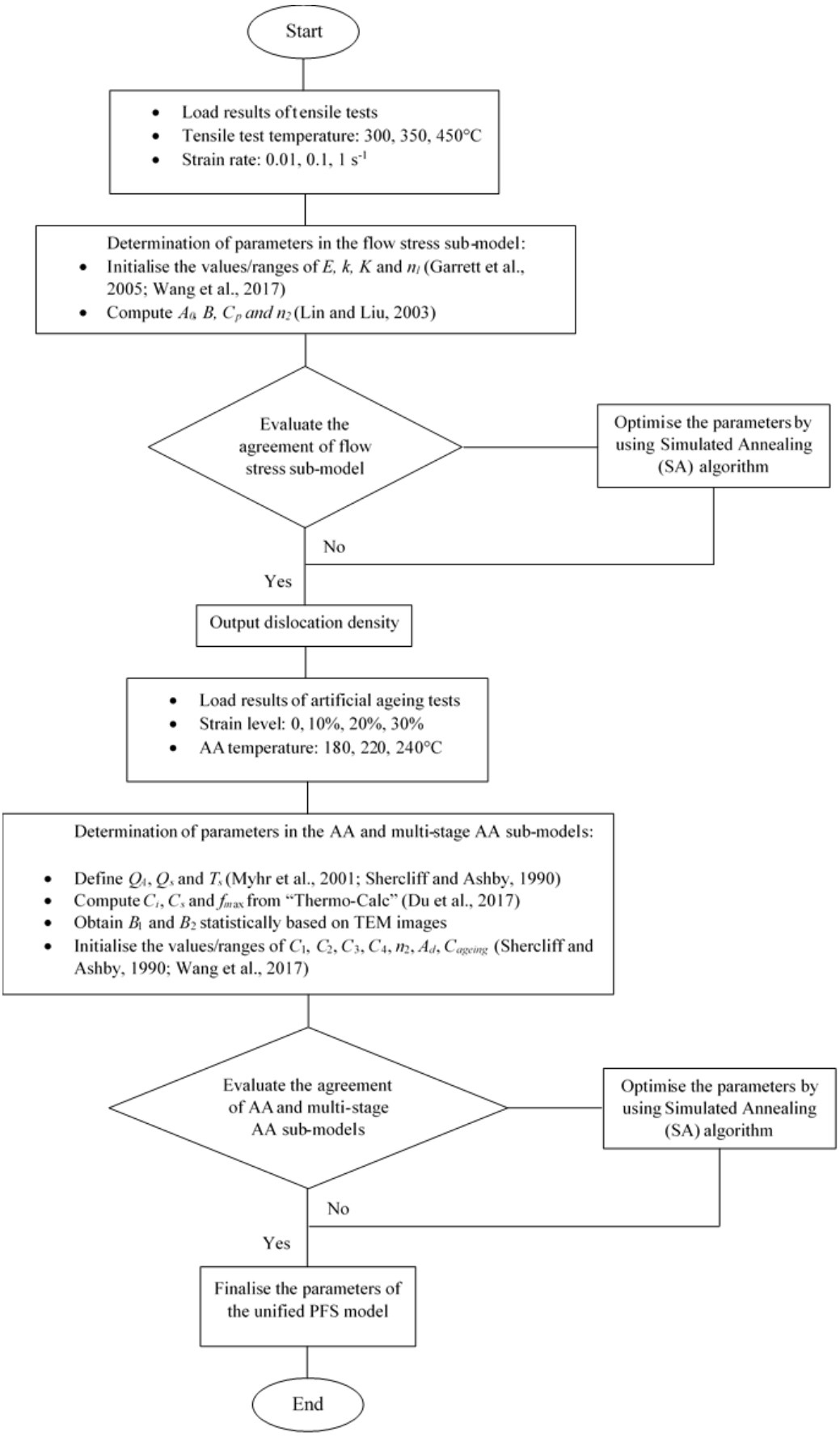
Start
Load results of tensile tests
Tensile test temperature: 300, 350, 450°C
Strain rate: 0.01, 0.1, 1 s-1
Determination of parameters in the flow stress sub-model:
Initialise the values/ranges of E, k, K and n1 (Garrett et al., 2005; Wang et al., 2017)
Compute A1, B, Cp and n2 (Lin and Liu, 2003)
Evaluate the agreement of flow stress sub-model
Optimise the parameters by using Simulated Annealing (SA) algorithm
No
Yes
Output dislocation density
Load results of artificial ageing tests
Strain level: 0, 10%, 20%, 30%
AA temperature: 180, 220, 240°C
Determination of parameters in the AA and multi-stage AA sub-models:
Define Q1, Qs and Ts (Myhr et al., 2001; Shercliff and Ashby, 1990)
Compute C1, Cs and fmax from "Thermo-Calc" (Du et al., 2017)
Obtain B1 and B2 statistically based on TEM images
Initialise the values/ranges of C1, C2, C3, C4, n2, Ad, Cageing (Shercliff and Ashby, 1990; Wang et al., 2017)
Evaluate the agreement of AA and multi-stage AA sub-models
Optimise the parameters by using Simulated Annealing (SA) algorithm
No
Yes
Finalise the parameters of the unified PFS model
End